Thermal state of the Guaymas Basin derived from gas hydrate bottom simulating reflections and heat flow measurements

Authors: Sudipta Sarkar[1*], Manuel Moser[2], Christian Berndt[3], Mechthild Doll[4], Christoph Böttner[3], Wu-Cheng Chi[5], Dirk Klaeschen[3], Christophe Galerne[6], Jens Karstens[3], Sonja Geilert[3], C. Mortera-Gutierrez[7], Christian Hensen[3]

Affiliations:

[1]Indian Institute of Science Education and Research, Dr. Homi Bhabha Road, Pune 411008, India

[2]Centre for Arctic Gas Hydrate (CAGE), Department of Geosciences, UiT-The Arctic University of Norway, Tromsø, Langnes, 9037, Tromsø, Norway

[3]GEOMAR Helmholtz Centre for Ocean Research Kiel, Wischhofstraße 1–3, 24148 Kiel, Germany

[4]MARUM – Center for Marine Environmental Sciences and Faculty of Geosciences, University of Bremen, Klagenfurter Strasse 4, 28359 Bremen, Germany

[5]Institute of Earth Sciences, Academia Sinica, 128 Academia Road, Section 2, Nankang, Taipei 11529, Taiwan

[6]Department of Geosciences, University of Bremen, Klagenfurter Strasse 2-4, 28359 Bremen

[7]Instituto de Geofísica, Universidad Nacional Autónoma de México, Circuito Exterior, Ciudad Universitaria, Coyoacán, D.F., C.P. 04510, Mexico

*Correspondence to: sudipta@iiserpune.ac.in

Key points:

- A regional bottom-simulating reflection (BSR) in the Guaymas Basin indicates a widespread occurrence of gas hydrates.
- The BSR derived thermal gradients show wavy patterns farther away from the spreading centre, indicating strong lateral heat flow variations.
- High sedimentation suppresses heat flow, while recent magmatic intrusion and fluid advection increase heat flow.

Abstract: Seafloor heat flow provides information about the thermal evolution of the lithosphere, the magnitude and timing of volcanic activity, and hydrothermal circulation patterns. In the central Gulf of California, the Guaymas Basin is part of a young marginal spreading rift system that experiences high sedimentation (1–5 km/Myr) and widespread magmatic intrusions in the axial troughs and the off-axis regions. Heat flow variations record magmatic and sedimentary processes affecting the thermal evolution of the basin. Here, we present new seismic evidence of a widespread bottom-simulating reflection (BSR) in the northwestern Guaymas Basin. Using the BSR depths and thermal conductivity measurements, we determine geothermal gradient and surface heat flow variations. The BSR-derived heat flow values are less than the conductive lithospheric heat flow predictions for mid-oceanic ridges. They suggest that high sedimentation (0.3–1 km/Myr) suppresses the lithospheric heat flow. In the central and southeastern regions of the basin, the BSR-derived geothermal gradient increases as the intruded magmatic units reach shallower subsurface depths. Thermal modeling shows that recent (<5000 years) igneous intrusions (<500 m below the seafloor) and associated fluid flow elevate the surface heat flow up to five times. BSR-derived geothermal gradients correlate little with the depth of the shallowest magmatic emplacements to the north, where the intrusions have already cooled for some time, and the associated hydrothermal activity is about to shut down.

Plain Language Summary: The mid-ocean ridge is a seafloor volcanic system where hot magma rises and creates a new ocean floor that gradually cools down as it spreads away from the magma rising centre. Sediments can bury the ocean floor, such as in the Guaymas Basin of the central Gulf of California. Heat flow measurements suggest that the accumulation of colder sediments may substantially lower seafloor temperatures below values expected for an ocean floor in an early spreading phase. These conditions are favourable for widespread methane entrapment in a solid ice-like compound, methane hydrate. We discover methane hydrates in extensive areas of the Guaymas Basin and use them to derive subsurface temperature gradients. The thermal profile away from the seafloor-spreading centre does not decline smoothly but rather undulates. We locate the hot spots representing the areas of fluid flow triggered by recent magmatic intrusions (~6–25 kyr) in the southern and central regions of the basin farther away from the magma rising centre. The northern part of the basin is relatively colder as the adjacent continent acts as a heat sink. There, intrusions that previously fuelled fluid circulation have been less active recently.

1. Introduction

1.1. Motivation and Objective

Surface heat flow variations in an oceanic basin provide insight into its thermal evolution (McKenzie, 1967), the magnitude, timing, and extent of magmatic activity (Skogseid et al., 1992), subsurface hydrothermal circulation patterns (Elder, 1965; Langseth & von Herzen, 1970; Davis et al., 1999; Kolandaivelu et al., 2020), and marine gas hydrate stability (Yamano et al., 1982). The thermal history has implications for hydrocarbon generation from organic-rich sediments (Simoneit and Lonsdale, 1982; Didyk and Simoneit, 1989). The heat source can strongly influence the onset of organic maturation and the volume of generated hydrocarbons. Voluminous magma intrusion into the sediments can elevate heat flow and result in rapid carbon transfer from the geosphere to the ocean and atmosphere causing global warming as suggested for the Palaeocene-Eocene Thermal Maximum (Svensen et al., 2004). Heating also facilitates the release of reactive dissolved organic matter critical for benthic microorganisms (Lin et al., 2017). The geothermal gradients strongly influence the microbial community composition that accounts for the diversity in the deep-sea ecosystem (Roussel et al., 2008; Teske et al., 2014).

This study focuses on the Guaymas Basin in the central Gulf of California (**Figure 1**), formed due to seafloor spreading (Lizarralde et al., 2007). The Guaymas Basin has several unique features. Rift-related magmatism leads to magmatic intrusions into organic-rich marine sediments (Einsele et al., 1980). High sedimentation (1–5 km/Myr, Calvert, 1966; Teske et al., 2021a) prevents the formation of a typical mid-oceanic ridge topography. Magmatic intrusions and hydrothermal activities are confined to the spreading centre and widespread in the off-axis regions (Lonsdale and Becker, 1985; Lizarralde et al., 2011). A continually high heat flow at the spreading centre is attributed to basaltic melts intruding into sediments (Einsele, 1985) and deeper magma sources. Convective processes, such as active hydrothermal circulation, result in complex thermal structures (Fisher and Narasimhan, 1991).

Seafloor heat-flow measurements directly estimate the thermal gradients (von Herzen and Maxwell M.E., 1959; Hyndman et al., 1979; Davis et al., 1999). However, these measurements are conducted at isolated locations and are susceptible to variations in topography, rapid sedimentation or erosion (Strasser et al., 2009), and transient bottom water temperature changes. Marine sediments host methane hydrates that form under high-pressure and low-temperature (Kvenvolden, 1993). The stability of methane hydrates in marine sediments is mainly affected by pressure and bottom water temperature conditions (Claypool & Kaplan, 1974; Sloan and Koh, 2008). Hydrate destabilization may lead to the release of the potent greenhouse gas methane leading to global climate warming. It is possible to estimate thermal gradient by determining the subseafloor depth of the base of gas hydrate stability (BGHS) and the temperature at that depth.

The BGHS is defined by the intersection of the hydrate phase boundary with the geothermal gradient. Free gas accumulates at the BGHS, and the strong seismic impedance contrast across the boundary causes a seismic reflection (Shipley et al., 1979; White, 1979). In regions with steady heat flow, the seismic reflection usually mimics the seafloor topography, and often crosscuts the host stratigraphy as a reversed-polarity reflection. The reflection is called a bottom-simulating reflection (BSR) (Shipley

et al., 1979; White, 1979). Heat flow variations (Ganguly et al., 2000), fluid flow (Haacke et al., 2009), changes in salinity (Hornbach et al., 2005), gas composition (Portnov et al., 2021), variations in sedimentation (Zander et al., 2017) and seafloor topography (He et al., 2007) may cause a deviation of the BGHS topography from the sea bottom topography, making the resulting reflection not strictly simulating the seafloor. Regardless of such deviation, we use the term BSR as it is more commonly used and is widely recognized in the scientific community.

We use several seismic reflection profiles from the Guaymas Basin to map out the BSR. The information on the depth of the BSR below the seafloor, together with the knowledge of the hydrate composition and the associated phase boundaries, bottom-water temperature, and thermal conductivity, allow estimating the geothermal gradient and the heat flow (Shipley et al., 1979; Yamano et al., 1982). The subtle variations in the regional thermal gradient help elucidate different thermal and geological factors influencing surface heat flow, such as conductive heat loss after a break-up, changes in sedimentation rate, and hydrothermal activity due to magmatic intrusions into the sediments. Our objective is to use dense and widespread temperature data to investigate the driving forces of processes causing thermal anomalies in the off-axis region of a young oceanic basin and to unravel the heat transfer mechanisms involved in the thermal perturbation over a regional scale. We use numerical simulations to determine the effects of sill intrusions, sedimentation, and off-axis distance on conductive heat transport and differentiate them from advective heat transport along focused fluid flow conduits.
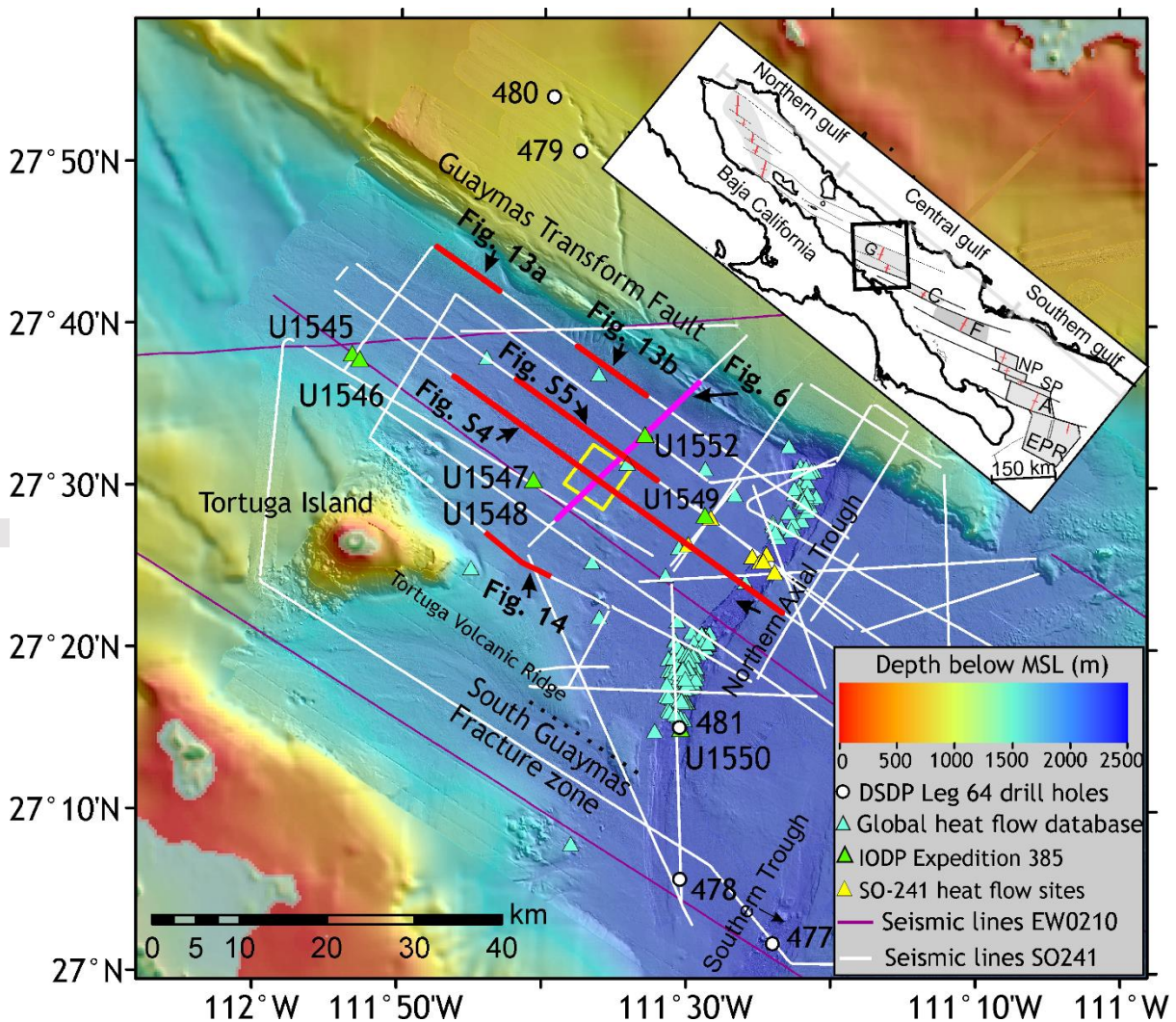
Figure 1. *Overview map with bathymetry highlighting the northern and southern Guaymas axial troughs and the transform system. The multibeam bathymetric data is derived from the bathymetric data provided by the UNAM-LUCO group and the bathymetric data acquired during the SO241 cruise. The base map also shows the 2D seismic lines (SO241 and EW0210). Heat flow measurement stations are shown by triangles. The inset shows the major structural elements in the Gulf of California and the location of the Guaymas Basin (after Padilla y Sánchez et al., 2013). Central and Southern gulf spreading centres are labelled, G– Guaymas, C–Carmen, F–Farallon, NP–North Pescadero, SP–South Pescadero, A– Alarcon, EPR–East Pacific Rise.*

2. Geological setting

The Gulf of California represents an oblique rift system with several seafloor-spreading centres connected by transform faults (Larson et al., 1968). The spreading axis of the Guaymas Basin is represented by northern and southern axial troughs separated by northwest-southeast striking transform faults (Einsele, 1985; Lonsdale and Becker, 1985). The Guaymas Basin initially evolved as a half-graben before the onset of ocean spreading (Aragón- Arreola et al., 2005). The Guaymas Transform Fault marks the northern boundary, along which the Pacific Plate slips northwest with respect to the adjacent North American Plate at ~48 mm/yr (**Figure 1**). Based on the width of the accreted igneous crust and the spreading rate across the basin, Lizarralde et al. (2007) estimated ocean spreading initiated ~6 Myr ago. The Tortuga Island is a tholeiitic shield volcano built on the Tortuga Volcanic Ridge (Figure 1, Batiza, 1978; Fabriol et al., 1999).

Mixed siliceous and turbiditic sediments are deposited in the axial troughs and rift flanks (Calvert, 1966; Einsele and Kelts, 1982). The southeastern off-axis and the spreading centres receive terrestrial sediments from the Yaqui and Mayo rivers (Kluesner et al., 2014). Mass transport complexes resulting from slope instability have been recognized in the northern axial trough (Berndt et al., 2016). The average sedimentation rate is 1 km/Myr in the northwestern Guaymas off-axis, with local variations (0.285–3.5 km/Myr, Geilert et al., 2018; Teske et al., 2021a). A low sedimentation rate of 0.285 km/Myr signifies a lack of terrestrial input in those regions (Teske et al., 2019). Aragón-Arreola et al. (2005) developed the seismic stratigraphic framework of the northwestern Guaymas Basin. The wedge-shaped sedimentary succession filling the initial half-graben structure thickens towards the Guaymas Transform Fault. The mound-shaped contourites immediately west of the Guaymas Transform Fault indicate along slope flowing bottom currents control sedimentation (Aragón- Arreola et al., 2005).

Many heat flow surveys were conducted in the northern and southern axial troughs (Lawver et al., 1973; Williams et al., 1979; Lonsdale and Becker, 1985; Fisher and Becker, 1991; Teske et al., 2016; Teske et al., 2021a). They indicated broad areas with high heat flow result from a combination of conductive heat transfer and hydrothermal venting caused by the intrusion of basaltic magma into turbidites and hemipelagic sediments in the axial trough (Einsele et al., 1980; Curray et al., 1982). The shallowest sediments in the Guaymas Basin have ~3–4% organic carbon content (De la Lanza-Espino and Soto, 1999). The presence of gas and folded structures indicates hydrocarbons generated by thermogenic reactions and sediment deformation related to magmatic intrusions (Aragón- Arreola et al., 2005). Numerous hydrothermal vents are also present in the northwestern Guaymas Basin (Lizarralde et al., 2011; Teske et al., 2019). While present-day sill-intrusion-induced hydrothermal activity continues in the axial trough, the off-axis magmatic and hydrothermal activity have a complex evolution, such as an initial active venting that transits through intermediate-stage cooling and eventually becomes extinct (Geilert et al., 2018; Teske et al., 2019).

3. Data and Method

3.1. 2D Multichannel Seismic (MCS) and Parasound Data

We collected MCS data during expedition SO241 of the Research Vessel Sonne in the Guaymas Basin in June 2015 (**Figure 1**). MCS data were collected using a Geometrics GeoEel streamer of variable active lengths, such as 150, 162, 175, and 187 m with 96, 104, 112, and 120 channels, respectively. The hydrophone group spacing was 1.56 m. The seismic source signal was generated by two generator-injector (GI) air guns, each with a volume of 210 cubic inches or 3.44 l (1.72 l

generator and 1.72 l injector). The air guns were operated in harmonic mode at a tow depth of 2 m. The shot interval was 7 s, resulting in a mean shot point distance of 12 m. The recording time was 4 s, and the sampling rate was 1 ms. Seismic data processing included common mid-point (CMP) binning with a CMP bin spacing of 3.125 m; bandpass filtering using an Ormsby filter with corner frequencies of 20, 45, 250, and 400 Hz; normal move-out correction (NMO); and true amplitude recovery. The NMO-corrected gathers were stacked, and subsequently, a post-stack Stolt migration with 1500 m/s velocity was carried out. In addition to the SO241 seismic lines, we also used MCS data collected during the Maurice Ewing PESCADOR expedition EW0210 in 2002 (Lizarralde et al., 2007). During that expedition, shots from the air gun array were fired at 100-m intervals and recorded with a 6-km-long, 480-channel streamer at a sampling rate of 4 ms and group spacing of 12.5 m. We sorted the data into a 6.25-m-spaced CMP domain. Pre-processing steps included noise suppression, F- K demultiple to attenuate water- bottom multiple. We carried out velocity analysis and Kirchhoff pre-stack time migration in the common offset gathers and generated the final stack. During the cruise SO241, we also collected hull-mounted sub-bottom profiler 18-kHz parametric sediment echosounder (PARASOUND) data using chirp pulses. We generated the envelope attribute (Taner et al., 1994) with the PARASOUND profiles. We interpreted the seismic profiles and identified key seismic horizons and seismic anomalies associated with magmatic emplacements, fluid migration, and gas hydrate.

3.2. Multibeam Bathymetric Data
During the SO241 cruise, the Kongsberg Simrad EM 122 system recorded multibeam bathymetric data over a depth range of 50–2060 m. The sonar frequency of the system is 12 kHz, and it operates with 864 beams with an angular coverage of 150°. Sound velocity profiles were collected during the cruise. Sound velocity corrections were automatically applied to bathymetry data during data acquisition. Data were corrected for the ship's motion and navigation. We used the MB-System software to process the data. Data processing consisted of cleaning the data, such as rejecting incoherent values. The data were gridded with a cell size of 20 m.

3.3. Heat flow measurements from the cruise SO241 and Global Heat Flow database
We conducted 21 heat flow measurements during SO241 (see Berndt et al., 2016). Temperatures were measured using miniaturized temperature loggers attached to a 5 m-long heat flow lance and a 7.2 m and 12.2 m-long gravity corer. The temperature was logged at a sampling rate of 1 s. The absolute accuracy of the measurement is ~0.1 K, and relative temperature resolution is 0.001 K. The temperature measurements may be affected by poor contact of the heat flow probe to the sediments, a non-vertical penetration into the seafloor, and compression effects due to heavy gravity corer. The high sedimentation rates can affect the heat flow values in the Guaymas Basin as prolonged high sedimentation may reduce measured geothermal gradients by 10–30% from the steady-state geothermal gradient (Berndt et al., 2016). Therefore, the actual steady-state geothermal gradients could be higher than the measured values (Shipley et al., 1979; Lawver and Williams, 1979; Fisher and Becker, 1991). A topographic correction was not applied to the thermal lance data because the heat flow measurement sites in the northwestern Guaymas Basin are relatively flat (**Figure 1**).

We used the KD2 Pro Needle Probe instrument to measure thermal conductivity on recovered core material from each measurement site. The probe was inserted into the sediments, and heated. The thermal conductivity was determined by measuring the increase and decay of temperature with time. Data processing was conducted following the method described by Hartmann and Villinger (2002). **Supporting Table S1 (Supporting Information)** shows the previously unpublished thermal gradients and thermal conductivity measurements from the northwestern off-axis regions. Additionally, we have also included the conductivity values from the Global Heat Flow Database and the results from the IODP Expedition 385 (Teske et al., 2021a, b). The measured conductivity values of shallow marine sediments range from 0.678 to 0.739 W/mK, with an average value of 0.73 W/mK. The conductivity of the sediments depends on pressure and temperature. Since we measured conductivity after recovering the core materials, thermal conductivity values likely differ from in situ conditions. We did not apply a correction but are aware of the possible error. Ratcliffe (1960) suggested a correction of 1% per 1.8 km water depth to the measured sediment conductivities at atmospheric pressure conditions since conductivity increases due to pressure increase. There is a 6%

increase in conductivity for sediment samples at a deep ocean-bottom temperature at 4° C compared to a temperature at 25° C. Thermal conductivity also depends on water content. We assume the water loss is negligible considering the cohesive diatomaceous clay-rich sediments.

3.4. Numerical sediment heat transfer simulations

We performed heat transfer simulations for the magma emplaced within sediments using the 2-D finite difference solver HYDROTHERM (**Supporting Text S1, Supporting Table S2**). We have modeled the thermal impact of the magmatic intrusions into the sediments (**Supporting Text S1**), by varying the thickness of the intrusive units (50, 100 m) and emplacement depths (350, 500, and 900 mbsf) to understand their impact on the surface heat flow. Permeability of the sediments influence the fluid flow patterns (**Supporting Text S1**). Permeability of sediments in the Guaymas Basin is likely to be less than 10^{-15} m^2 (Fisher and Narasimhan, 1991). In addition, we performed one-dimensional heat transfer simulations to determine the effect of sedimentation on surface heat flow using the modeling code SlugSed (Hutnak & Fisher, 2007). The model uses a deforming finite-difference grid to predict surface heat flow. The model evolves as the sediment-basement interface subsides, creating accommodation space where sediment accumulates and compacts by a pre-defined porosity-depth function. The parameters used in SlugSed are shown in **Supporting Table S3**.

4. Results

4.1. Bottom Simulating Reflections (BSR)

We identify stratigraphy-crosscutting, reversed polarity seismic reflections in the northern, southeastern, and western off-axis regions of the Guaymas Basin that we interpret as BSRs (**Figures 2, 3a**). Previously, Lonsdale (1985) identified BSRs on the Guaymas Transform ridge. But our new data show a more extensive occurrence of BSRs. The northern BSR region is located immediately south of the Guaymas Transform margin and represents the largest aerial extent of BSRs among the three regions. The western BSR region is approximately 25 km northwest of the Tortuga Island. The physical presence of gas hydrate was confirmed in a gravity core collected during the cruise SO241 (**Figure 2**, Geilert et al., 2018). Enhanced reflection amplitudes and predominant reduction of low frequencies below the BSR indicate the presence of free gas (**Figure 3a**). In most profiles, the BSR is parallel to the seafloor topography (**Figures 3a, 3b, and 3c**).

The strata-crosscutting character of the BSR is also seen in PARASOUND profiles, in which the BSR is evident as a high-amplitude reflection with seismic blanking underneath (**Figure 3b**). Locally, the BSR topography deviates from the seafloor topography (**Figure 3d**) and its continuity is disturbed by conical mounds and near-vertical seismic chimney structures, which show lower reflection strength than the surrounding regions. The sub-seafloor BSR depth shows considerable variations (**Figure 2**) between 47 m below seafloor (mbsf) towards the central area of the basin and 75 mbsf in the off-axis region immediately southwest of the Guaymas Transform margin.
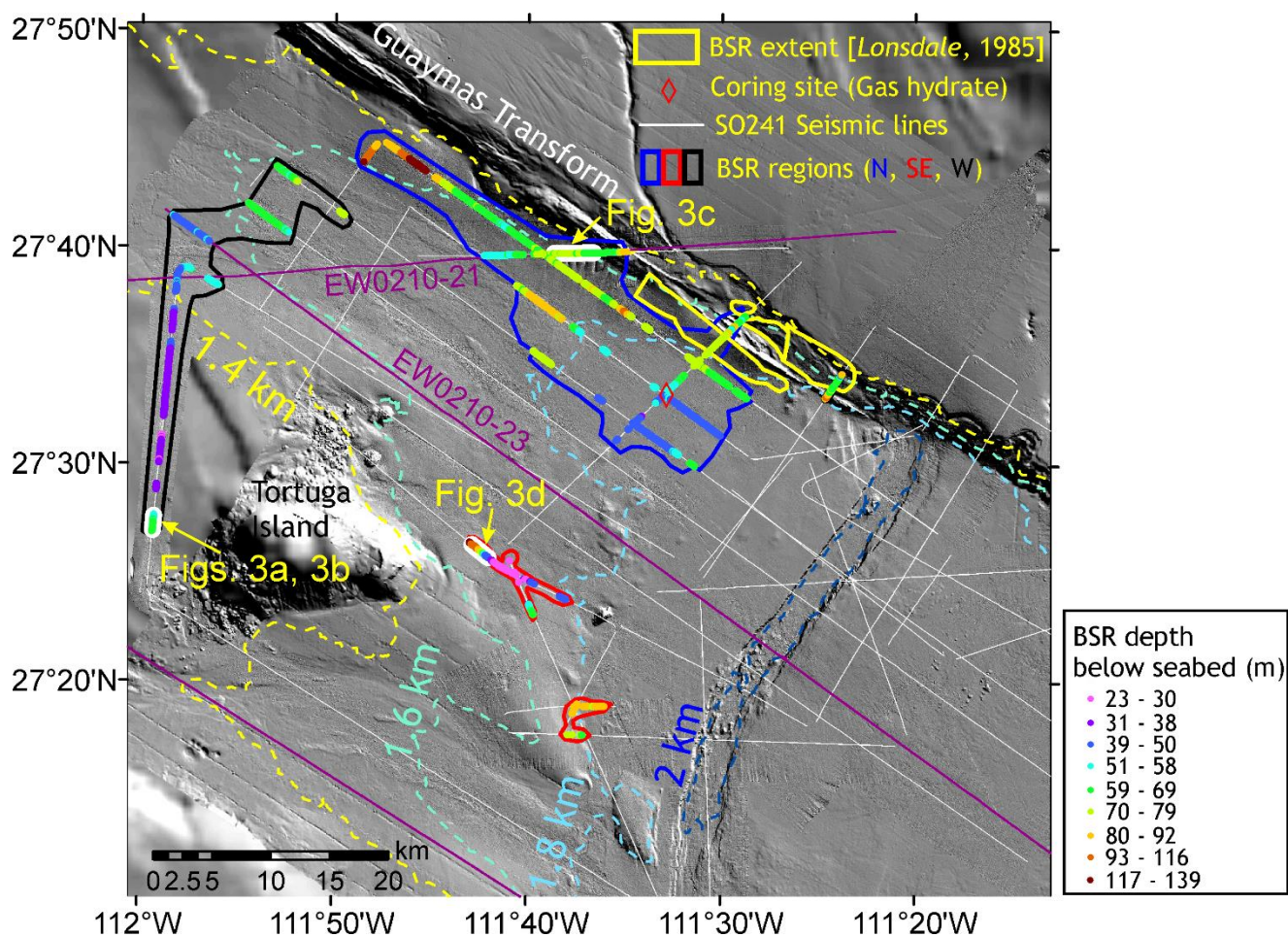
Figure 2. *BSR regions and the depth of the BSR below the seafloor. Gas hydrate was recovered from a core in the northern BSR region during the cruise SO241.*
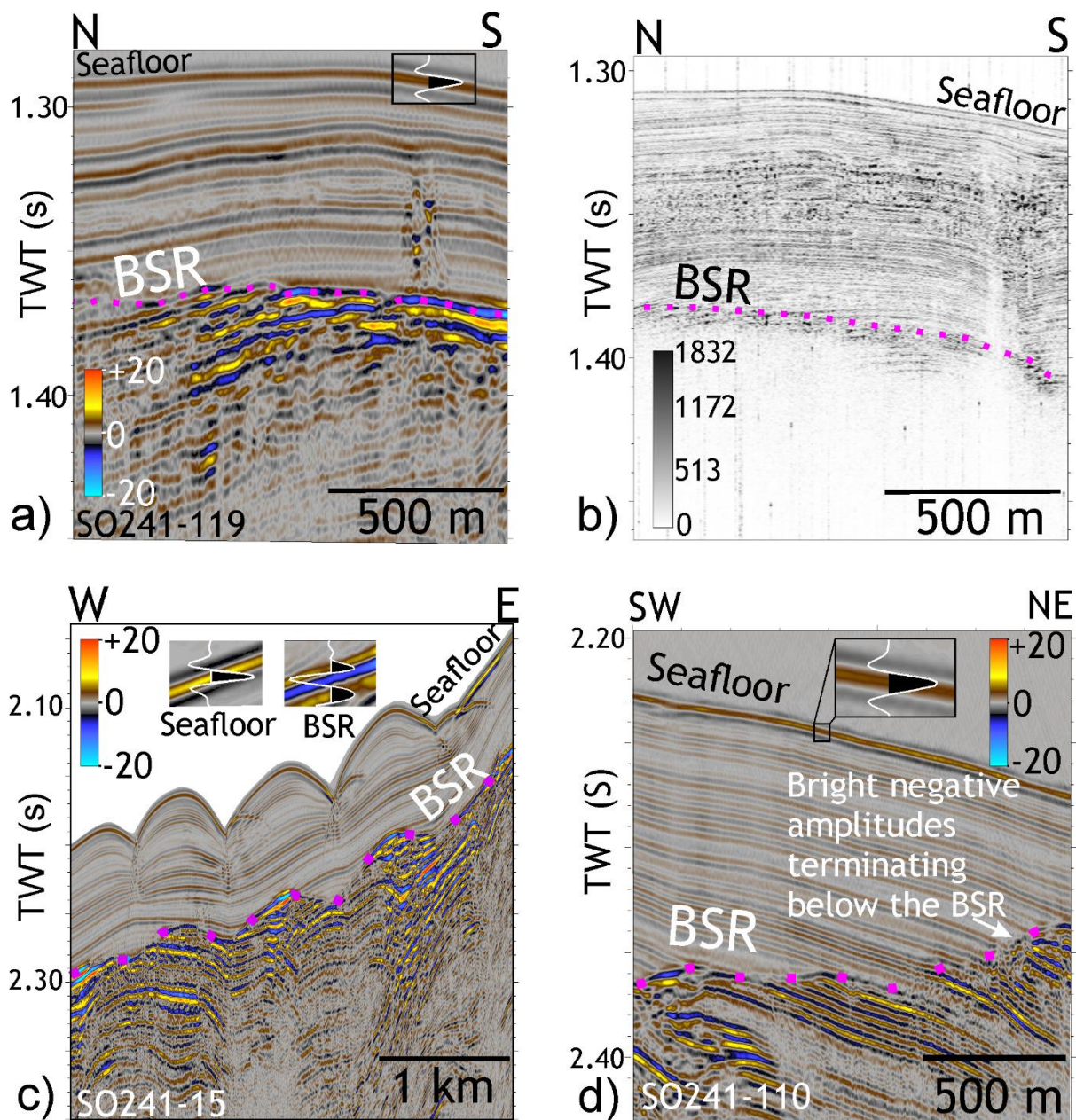
Figure 3. *Seismic expressions of BSR in northwestern Guaymas Basin off-axis. (a) The airgun seismic line SO241-119 shows a reversed polarity, crosscutting BSR and reflection brightening below the BSR. (b) A Parasound profile parallel to SO241-119 (Figure 3a) shows amplitude fading below the BSR. The parasound data is in the form of a positive-only envelope function. (c) Seismic line SO241-15 shows hummocky morphology at the seafloor, and the BSR mimics the seafloor. Below the BSR, reflection brightening is due to the presence of gas. (d) The BSR does not mimic the seafloor topography in the seismic line SO241-110. The bright negative amplitude reflections terminating below the BSR are due to gas. The seismic line locations are shown in Figure 2.*

4.2. Geothermal gradient derived from the BSR, uncertainty and comparison with field measurements

Considering the BSR as the base of the gas hydrate stability, we estimate a BSR-derived geothermal gradient based on the method established by Yamano et al. (1982), assuming a steady-state geothermal gradient. The depth to the BSR below the seafloor in two-way time (TWT, s) is converted to depth (m) by using an average velocity of 1600 m/s for the sediment column from the seafloor to

the BSR. We convert the BSR depths to pressure, assuming a hydrostatic model for sediment pore pressure. We use the seafloor temperature (T_{SB}) from the measured bottom-water temperature variation with depth during the cruise SO241 (**Supporting Figure S1**). The temperature at the BSR (T_{BSR}) is determined from the pressure- temperature conditions for the phase boundary of pure methane in seawater with a salinity of 35‰. We generate the hydrate stability curve using the CSMHYD program by Sloan (1998). We derive the geothermal gradient by using the formula (T_{BSR}-T_{SB})/z, where z is the depth of the BSR below the seafloor. The boxplot shows the variation in geothermal gradients in the three regions (**Figure 4**). The southeastern region shows the highest BSR-derived geothermal gradient (**Figures 4 and 5**), ranging between 106° and 650° C/km and with a median of 372° C/km. Such a high geothermal gradient is comparable with the values reported in the axial troughs (Fisher and Becker, 1991).

We combine the SO241 heat flow measurements and the Global Heat Flow Database data. As heat flow is the product of thermal conductivity and the geothermal gradient, we calculated heat flow using the BSR-derived geothermal gradient, and average thermal conductivity of the shallow marine sediments (0.73 W/mK). To obtain information on the possible variability we compared the BSR-derived geothermal gradient with the field measurements, where the sites are closest to the seismic lines (**Supporting Table S4**). The BSR-derived geothermal gradients vary within 5–12% of the measured geothermal gradients.
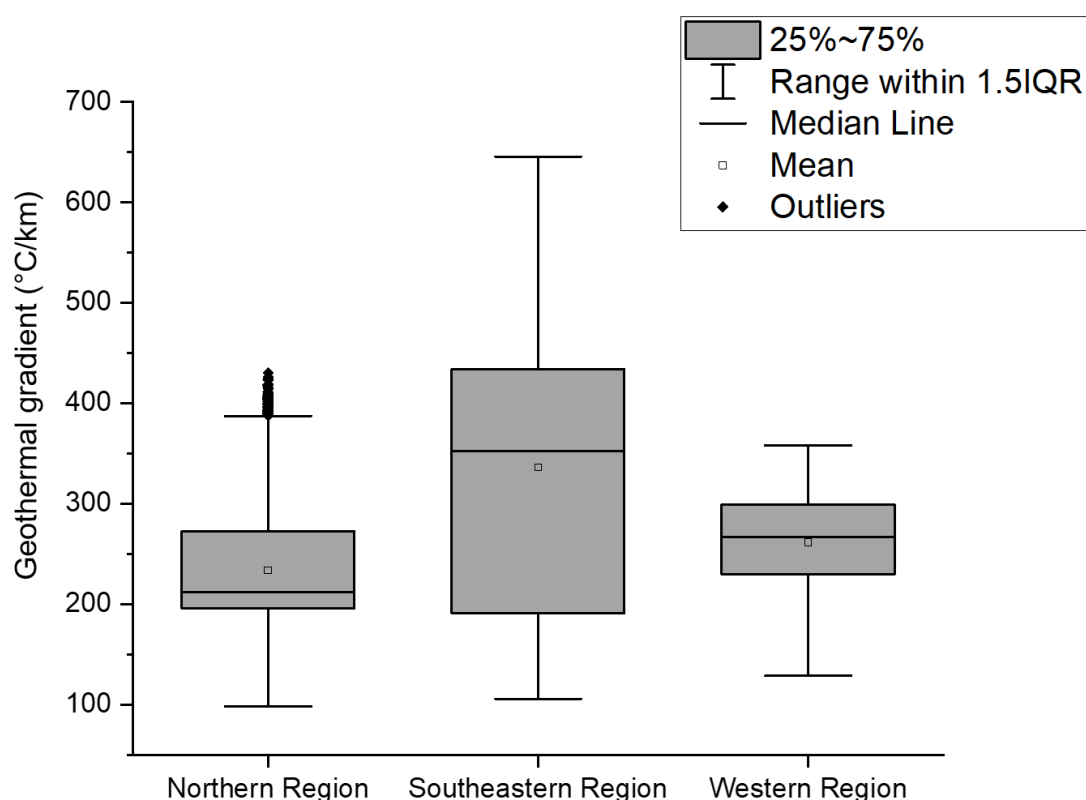

Figure 4. *Boxplots of geothermal gradients derived from the depth of the BSR. The southeastern BSR region shows a large range and higher geothermal gradients than the other regions.*
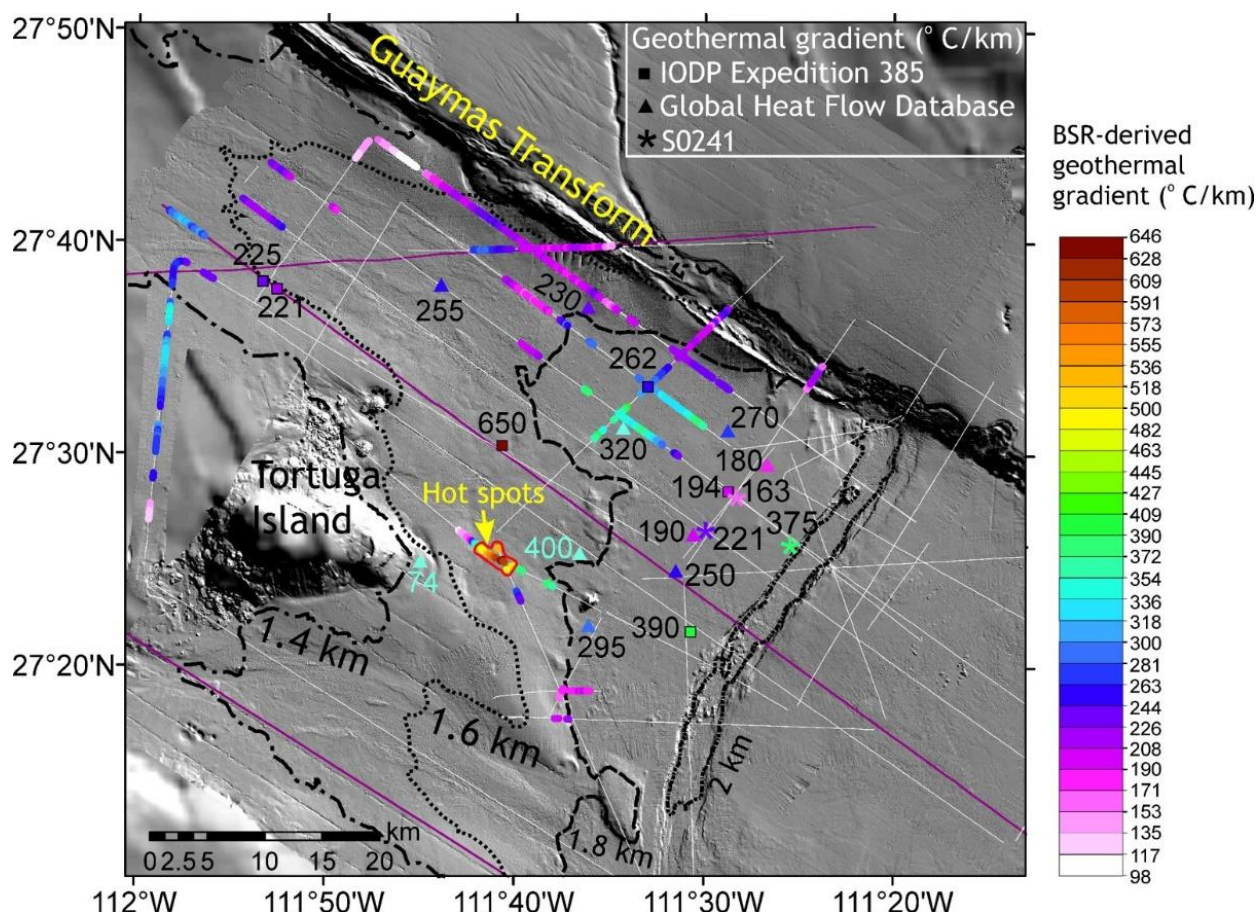
Figure 5. *Spatial variations of geothermal gradient derived from the BSR. The red polygon indicates the anomalous hot spots (see also **Figure 8b**). Geothermal gradients from various surveys and the IODP Expedition 385 are also shown.*

4.2.1. Errors associated with BSR-derived heat flow

BSR-derived heat flow has several uncertainties (e.g. Chi and Reed, 2008). First, there are errors associated with determining the subseafloor depth of the BSR. The picking accuracy for the BSR is limited by the vertical resolution of seismic data, typically one-fourth to one-half of the dominant wavelength resulting in approximately ~5 m resolution for the top 300 m of the subsurface. This results in a relative geothermal gradient error of 3–4.5%.

We have considered an average P-wave velocity of 1600 m/s for converting seismic travel-times to depth. The compressional velocities derived from the seismic profile EW0210-21 show variations of ±5% within the top 150 m of the sedimentary column. The average P-wave velocity measured between 50 and 150 mbsf in the IODP Expedition 385 Site 1545 is 1525 m/s (Teske et al., 2021d). The errors associated with the velocities can cause variation in the sub-bottom BSR depth.

The North Pacific Intermediate Water flows between 500 and 1000 m depths, and the Pacific Deep Water flows at deeper depths (>1000 m) of the Guaymas Basin (Bray, 1988). Bottom water temperature for 1939–1983 shows no distinguishable seasonal variation of the Pacific Deep Water (Robles and Marinone, 1987). Therefore, the geothermal gradient estimation from the BSR depth should not be affected by seasonal changes in bottom water temperature.

The calculated temperature at the BSR is dependent on the choice of the hydrate stability curve considering seawater salinity (35‰). This is consistent with the measured salinities at the seafloor across all IODP sites from Expedition 385 (Teske et al., 2021a). We tested a range of gas compositions for hydrate phase stability. Methane in shallow marine sediments (<5 mbsf) is mostly microbial or mixed microbial and thermogenic in origin (Geilert et al., 2018). In IODP Expedition 385 Sites 1545, 1549 and 1552, methane is the dominant (99.68–99.97%) hydrocarbon gas in the top

~100 m of the sediment column (Teske et al., 2021d). We also consider two mixed-gas hydrate systems containing 91% methane, 8% carbon dioxide, and 1% ethane based on gas concentrations measured at 20 mbsf in the DSDP Hole 481A (Shipboard Scientific Party DSDP 64, 1982) and 98% methane, and 2% ethane based on measurements at 120 mbsf in the IODP Expedition 385 Site 1547 (Teske et al., 2021c). The presence of higher hydrocarbons increases the stability of the hydrate.

We assume hydrostatic equilibrium at a depth of the BSR since overpressure on large lateral scales is unlikely at shallow depth. A lithostatic pressure assumption considering the load of the sediments at a depth of BSR would yield a difference of 0.1–0.2° C/km. The density differences lead to a systematic increase of less than 1% (He et al., 2007).

We show how various uncertainties may affect the BSR derived geothermal gradient using an example in **Supporting Table S5**. The uncertainties in geothermal gradient related to the velocities are relatively small (±5%). The geothermal gradient estimate considering mixed gas hydrate composition is 7% higher compared to pure methane hydrate. The absolute error can increase by 13% considering a shallower BSR depth (e.g. 40 mbsf) and mixed hydrate model (98% methane, and 2% ethane). The measured thermal conductivities from the heat flow database and measurements conducted during the cruise SO241 show a variation of ±10%. The measured thermal conductivity values in IODP Expedition 385 Site 1545 vary between 0.6 and 0.8 W/mK in the top 200 m sediment column (Teske et al., 2021d). A thermal gradient of 280° C/km corresponds to a calculated heat flow of 204.4 mW/m^2, considering an average thermal conductivity of sediments as 0.73 W/mK. If thermal conductivity increased to 0.8 W/mK, heat flow would have also increased by 10%.

4.2.2. Topographic effects and their correction

The spatial variation of the BSR-derived surface heat flow reveals wavy patterns at some places that can result from topographic effects on subsurface temperatures. Complex topography causes thermal refraction of the heat flow below the seafloor, such as heat flow focusing over concave upward topography and defocussing over convex-upward topography. In those regions, topographic correction is required. The heat flux anomalies after topographic correction are likely due to geological factors, such as the advection of warm fluids that elevates heat flow or sedimentation that suppresses heat flow. The topographic effects are negligible where the seafloor is flat and the northwestern off-axis region reveals a relatively small variation in slope (average slope 2.6°, **Supporting Figure S2**). We carried out a three-dimensional (3-D) steady-state finite element analysis (FEA) to model the topographic effects on the heat flow in areas of complex bathymetry. The topographic modeling assumed a conductive heat flow model. We used ANSYS for meshing and solving the steady-state 3-D thermal conduction equation (**Figures S3a and S3b in Supporting Information**). Modeling shows a defocusing effect over the mound with low heat flow values (340 mW/m^2, **Supporting Figure S3a**), where the basal heat flow is 370 mW/m^2. We find high heat flow values at a depression on the Guaymas Transform margin and attribute it to the topographic focusing effect (**Figure 6**).
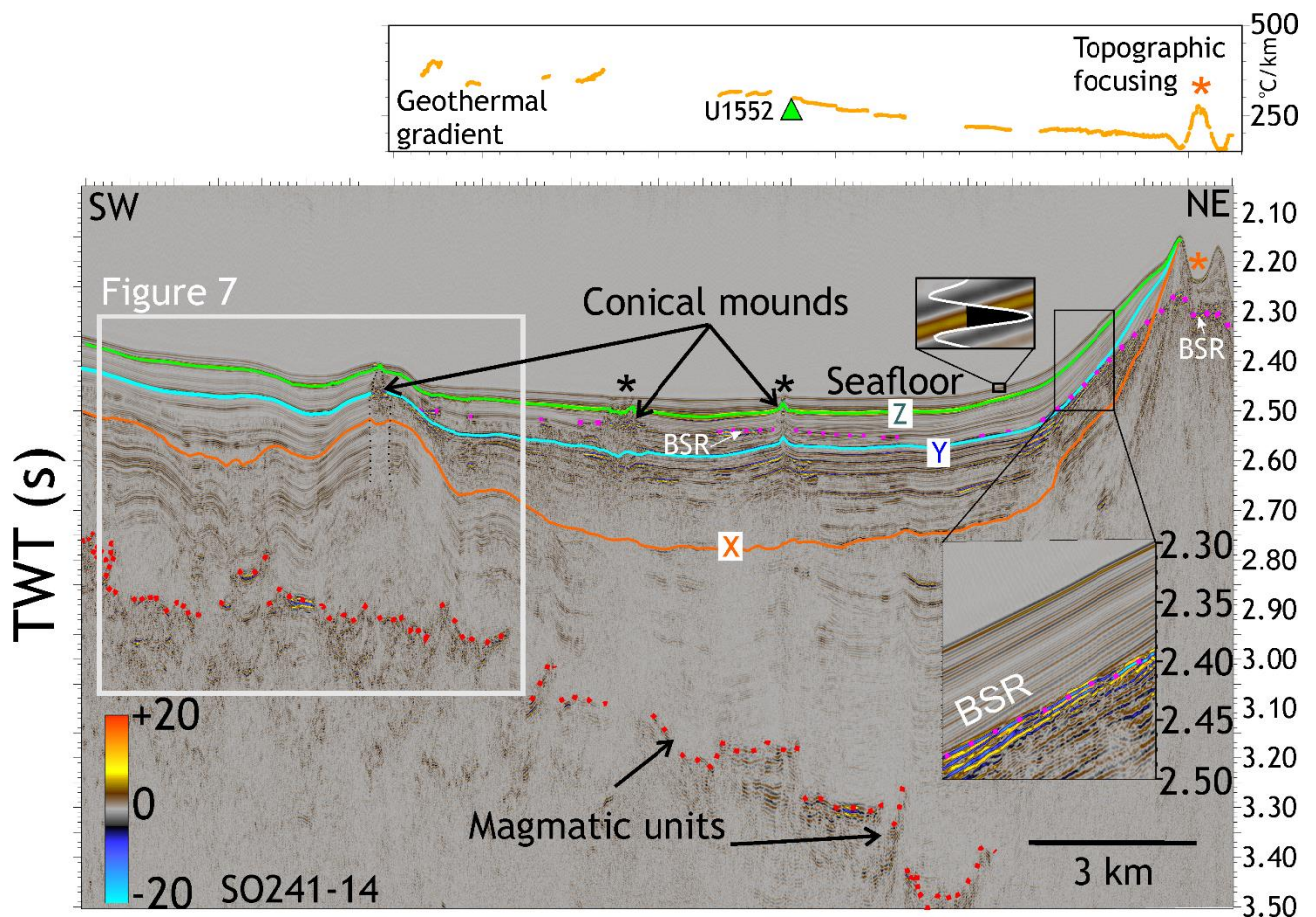
Figure 6. *The seismic line SO241-14 (location in Figure 1) shows the deepening of the magmatic units toward the northeast. The BSR derived geothermal gradients (top panel) gradually increase toward the southwest. Topographic focusing causes steepening of the geothermal gradients at a depression (marked by the orange asterisk). The conical mounds are hydrothermal vent complexes. The mounds shown by black asterisks are seen as high-backscatter features on the seafloor (Lizarralde et al., 2011). The green triangle (top panel) indicates the measured geothermal gradient at the IODP Site U1552 (IODP Expedition 385).*

4.3. Magmatic emplacements, their relative timing and relationship to BSR derived geothermal gradient

We identify several positive polarity bright reflections that are mostly sub-horizontal and concordant to the strata and show concave upwards geometries with marginal limbs that are discordant to the stratigraphy (**Supporting Figures S4 and S5**). The concave upward reflections are similar in appearance to the saucer-shaped sills previously reported in the Guaymas Basin (Lizarralde et al., 2011). The strong reflection amplitude at the top of the magmatic units is the result of a steep step-wise increase in seismic velocity and density, causing large impedance contrasts with the surrounding sediments. We have mapped the top of the shallowest magmatic units using the seismic lines (**Supporting Figure S6**).

We find seismic evidence for multiple stages of magmatic emplacements. Since we do not have radiometric dates for the igneous units, we examined the stratigraphic relationships of the magmatic units to the overlying strata to constrain the relative timing of magmatic emplacements. The reflector X, shallower than the top of the seismically resolvable shallow sill complexes, shows deformation, such as folds (**Figure 6 and Supporting Figure S4**). In the stratigraphic unit bounded by X and the seafloor, reflectors Y and Z serve as the base of several conical mounds (**Supporting Figure S5 and Figure 7**). A common seismic chimney connects the mounds (**Figure 7**). The chimney served as a pathway for rising fluids and gases (Geilert et al., 2018). Similar chimneys and vent complexes are observed off Norway (Schmiedel et al., 2017; Kjoberg et al., 2017; Omosanya et al., 2018; Roelofse et al., 2021), Scotland (Grove, 2013; Schofield et al., 2017; Hamilton and Minshell, 2019), Ireland (Magee et al., 2014) and northeast Greenland (Reynolds et al., 2017). The mounds show stratal onlap indicating a pause in hydrothermal activity and burial. We have assigned the ages of the horizons X,

Y, and Z to ~160–200 kyr, ~70–100 kyr, and ~6–25 kyr, respectively, based on their depth below the seafloor and assuming an average sedimentation rate of 1 km/Myr. Since the mounds result from hydrothermal fluid venting associated with magmatic emplacements, we infer that magmatic intrusions and resultant hydrothermal venting likely occurred during ~160–200 kyr, ~70–100 kyr, and ~6–25 kyr.

The cross-plot of the sub-bottom depth of the shallowest magmatic emplacements and BSR-derived geothermal gradient show large scatter in the geothermal gradient over the shallowest magmatic units that are emplaced at a depth of 300–400 mbsf (**Figure 8a**). The high geothermal gradients (>375° C/km) are clustered in the southeastern BSR region of the Guaymas Basin (**Figure 5**). On the quantile-quantile plot, those values sharply deviate from the normal trend at the upper end of the BSR-derived geothermal gradient range (**Figure 8b**). Geothermal gradient does not correlate with the depth of the shallowest magmatic units, if the topmost magmatic units are emplaced much deeper (>700 mbsf).
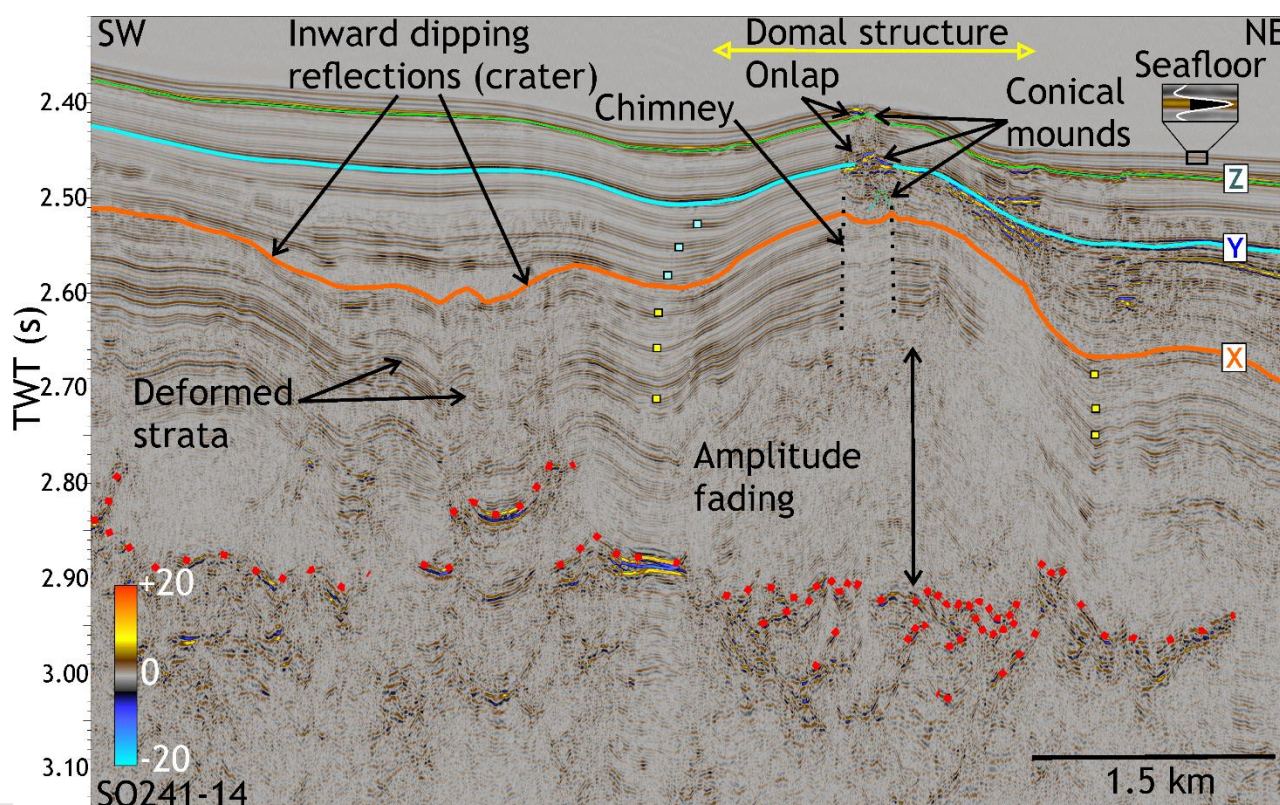

Figure 7. *The seismic line (location in Figure 6) showing sill intrusion-related deformation and presence of hydrothermal vent complexes at different stratigraphic levels. Stratal deformation and amplitude blanking are seen in the sedimentary unit overlying the inferred sills (red dots). Conical mounds stack up vertically and are connected by a vertical seismic chimney. The chimney is rooted at the zone of amplitude fading. The zone of amplitude fading is likely due to stratal disruption in the metamorphic aureoles around the sills. Crater and mound-shaped vent complexes occur on reflector X. The axial traces in the fold are near-vertical (small yellow squares) below the reflector X, but they (small cyan squares) dip away from the crest in the overlying layer. The unit bounded between X and Z is deposited above the fold after deformation ceased. They are warped due to differential compaction. The conical mounds are hydrothermal vent complexes formed by the release of hydrothermal fluids on the paleo-seafloor.*
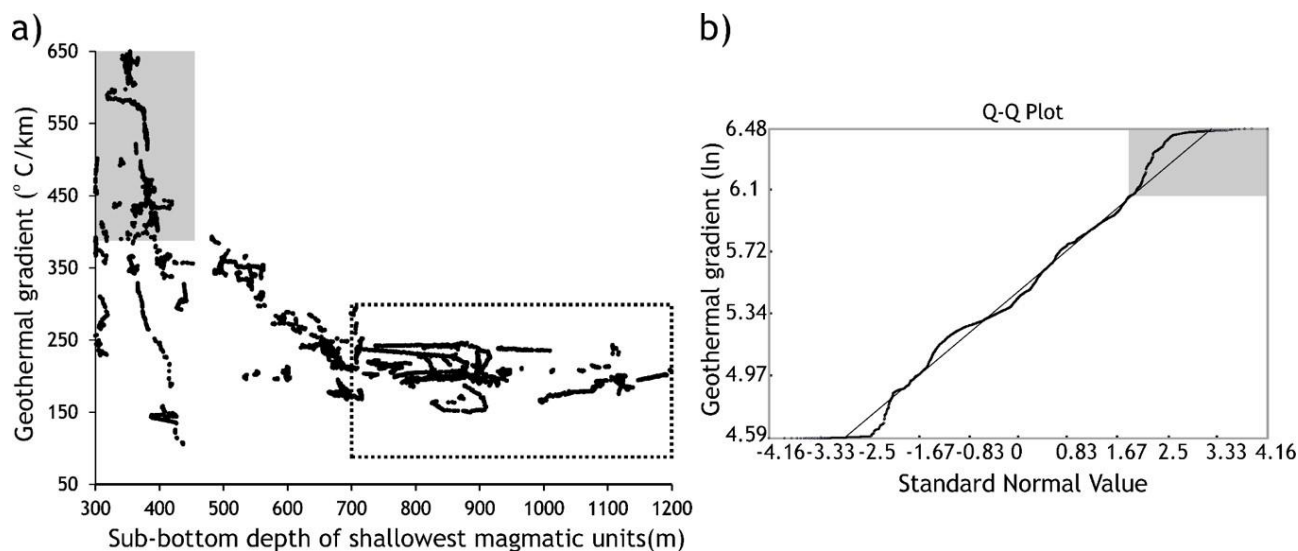
Figure 8. *The cross-plot between geothermal gradient and sub-bottom depth of the magmatic units and the quantile-quantile (Q-Q) plot of geothermal gradient. (a) The regions where the magmatic units are shallower than 450 mbsf show a large scatter in BSR derived geothermal gradients. There is no correlation between the geothermal gradients and the sub-bottom depth of the magmatic units in the regions where the magmatic emplacements are deep (>700 mbsf, rectangle with dotted outline). (b) On the Q-Q plot, log-transformed geothermal gradient values (>375° C/km, grey shaded area in Figures 8a and 8b) sharply deviate from the normal trend at the upper end of the BSR derived geothermal gradient range. They occur in the southeastern BSR region (hot spots in Figure 5).*

5. Discussion

The BSR-derived geothermal gradient variations depict the thermal state in the northwestern area of the Guaymas Basin. We consider several factors, such as the role of magmatic emplacements, the nature of heat transfer, the spatial variability in sedimentation, and the tectonic setting of the basin, for explaining the observed thermal pattern. Since the basin experiences a very high sedimentation rate, we have modeled the effect of sedimentation on expected seafloor heat flux based on a plate-cooling model considering the published spreading rate. The thermal anomalies after the sedimentation correction are then carefully analysed.

5.1. Relationship between intrusion depth and BSR-derived geothermal gradient

The BSR-derived geothermal gradients along a northeast-southwest profile in the northern BSR region show a decreasing trend from the central region of the northwestern basin to the Guaymas Transform Fault (**Figure 6**). The topmost magmatic units below the seafloor are much deeper in the region immediately south of the Guaymas Transform than at the central off-axis region (**Figure 6 and Supporting Figure S6**). Where the magmatic units are shallower than 700 mbsf, the cross plot between geothermal gradient and depth to the shallowest magmatic emplacements shows a linear trend of decreasing geothermal gradient with an increasing depth of the magmatic units (**Figure 8a**). Thermal modeling using HYDROTHERM provides insight into the thermal evolution of the sedimentary system influenced by sill intrusions at various depths. Modeling shows that heat transfer from the sill intrusion to the host sediments (permeability=10^{-16} m^2) results in a rise in the near-surface heat flow to a peak value, followed by its decline at the late stage cooling of magma (**Figure 9**, also see **Supporting Text S1**). For a shallow intrusion (350 mbsf), the temperature rise could be very rapid compared to a deeper sill (**Figure 9**). A deeper sill (900 mbsf) has to heat a thicker sediment column, thereby delaying the arrival of thermal perturbation to the surface. If the topmost intrusive units emplaced at different depths below the seafloor are coeval and of similar thickness (e.g., 100 m), the surface heat flow will be higher for the intrusions that are emplaced closer to the surface during the heating phase. Therefore, for the deeper magmatic intrusion, the attainment in the near-surface heat flow peak is delayed compared to a shallower sill intrusion. When the surface heat-flow attains a peak due to a deeper sill intrusion, the waning phase of surface heat flow has already

started for the shallower sills. A substantial difference in surface heat flow can arise due to variable depths of magmatic emplacements if a coeval set of intrusions are less than five thousand years apart (**Figure 9**).

The thermal modeling also sheds light on the time-scale of cooling of sills. The thermal anomaly associated with the deeply emplaced magmatic units could have dissipated if the intrusions have already cooled down completely. A lack of correlation between the geothermal gradient and the shallowest sill depths (>700 mbsf) likely indicates that the thermal anomaly associated with the magma injection has dissipated or that the intrusions are at least at a late cooling stage (e.g., >10 kyr after emplacement). In contrast, the shallower emplacements could be younger and show remnant thermal effects on the surrounding sediments. The explanation for the variation in heat flow with the depth of the topmost sill needs to be further tested when more constraints on the timing of sill intrusion become available, possibly from IODP Expedition 385 results.
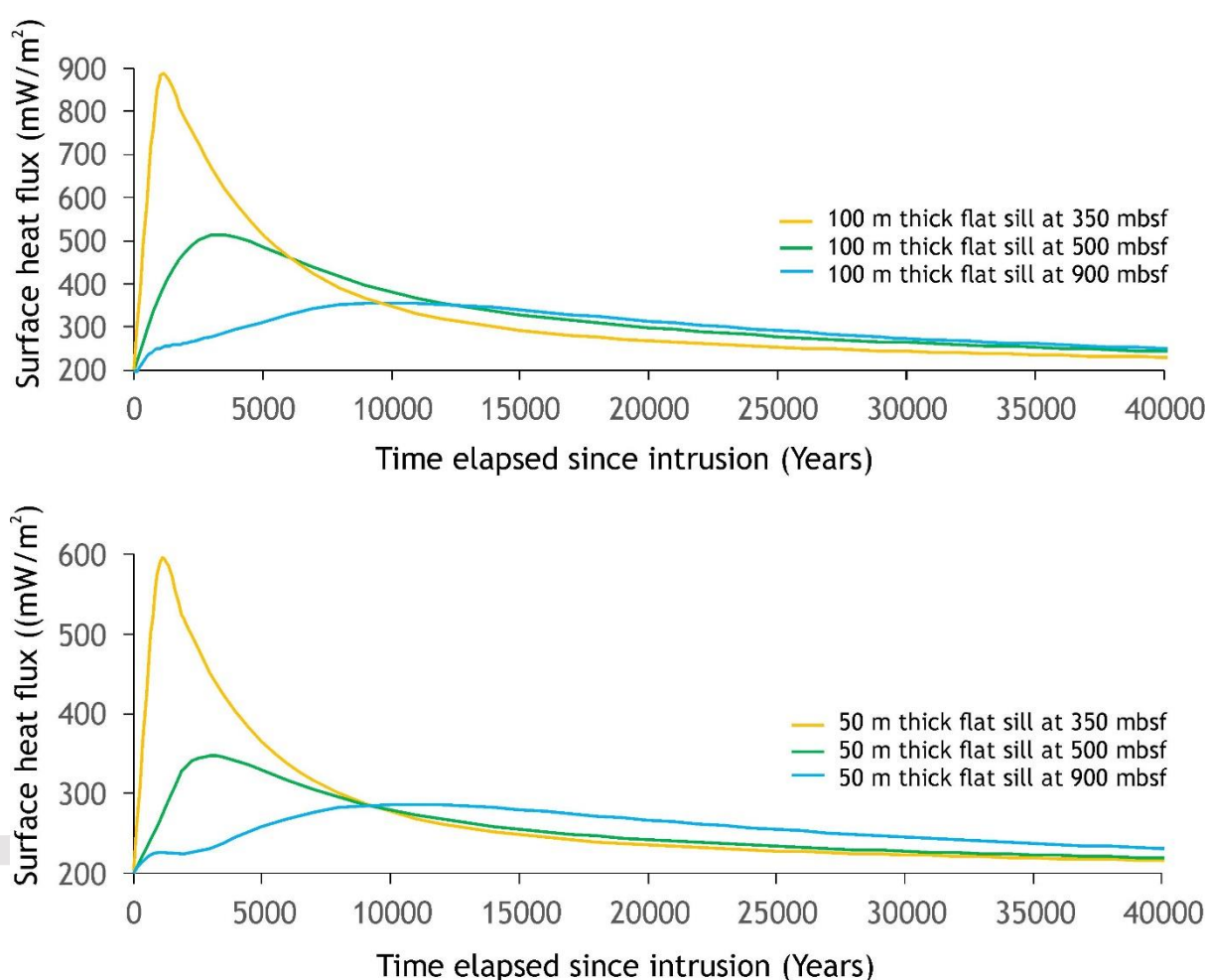

Figure 9. *Modeled variations in surface heat flow with time when a sill intrudes into the sedimentary column (permeability 10^{-16} m^2). The results are based on a 2-D heat transfer model using HYDROTHERM. The background heat flow is 200 mW/m². (Top) Surface heat flow variations for a 100 m thick sill emplaced at 300, 500, and 900 mbsf. Over the shallowest sill intrusion at 300 mbsf, the heat flow initially rises steeply from 200 mW/m² to 900 mW/m² and subsequently declines. Over the deeper sills (500, 900 mbsf), the arrival of the peak is delayed as the ascending thermal front travels a greater distance. (Bottom) Surface heat flow variations over a 50 m thick sill emplaced at 300, 500, and 900 mbsf.*

5.2. Effect of sedimentation

The derived heat flow values at the northern axial trough show a large scatter (**Figure 10**, Mean=1665 mW/m², minimum=21 mW/m², maximum=41634 mW/m², standard deviation=6795 mW/m²). Very

high heat flow could be due to upwelling hydrothermal fluids while cooling occurs at other sites from where heat is withdrawn. Hutnak and Fischer (2007) argued that thermal discharge through vent complexes and recharge along faults set up vigorous convection that can efficiently redistribute heat on the youngest (<0.1 Ma) oceanic crust. A 600 m-thick fractured basalt layer with high permeability and efficient conductivity (Nusselt number=1000) can reduce the surface heat flow by 80% and explain very low heat flow values (Hutnak and Fischer, 2007). The measured heat flow values show less scatter (Mean=175 mW/m^2, minimum=109 mW/m^2, maximum=276 mW/m^2, standard deviation=41 mW/m^2, **Figure 10**) outside the axial trough and between 3 km and 10 km away from the spreading centre (estimated spreading ages 200–400 kyr). Beyond 10 km from the spreading centre, the surface heat flow fraction, which is the ratio of BSR derived heat flow to the lithospheric heat input, gradually rises with crustal age in the northwestern parts of Guaymas Basin (**Figure 11**).
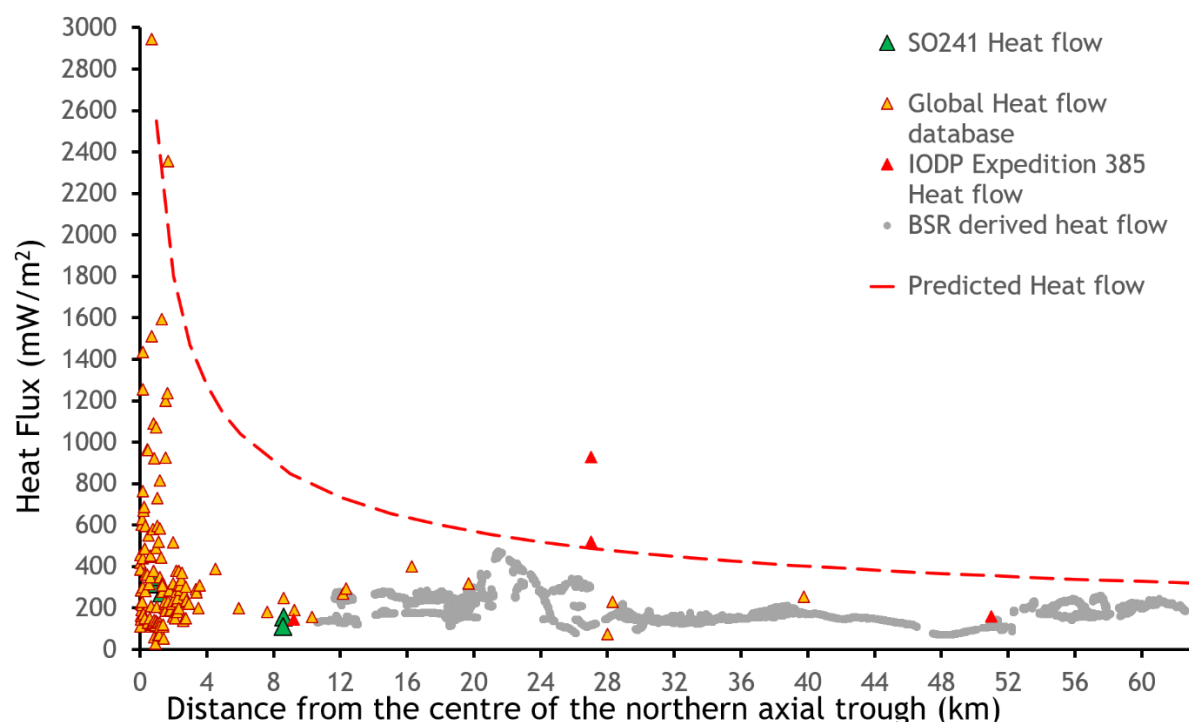

Figure 10. *Seafloor heat flow versus distance from the centre of the northern axial trough in the northwestern off-axis of the Guaymas Basin. The triangles demarcate the measured heat flow values from the global heat flow database, SO241 heat flow survey, IODP Expedition 385. The grey circles represent the BSR derived heat flow values. The locations of heat flow measurement stations are in Figure 1. The dashed line is the predicted heat flow (Lawver and Williams, 1979).*
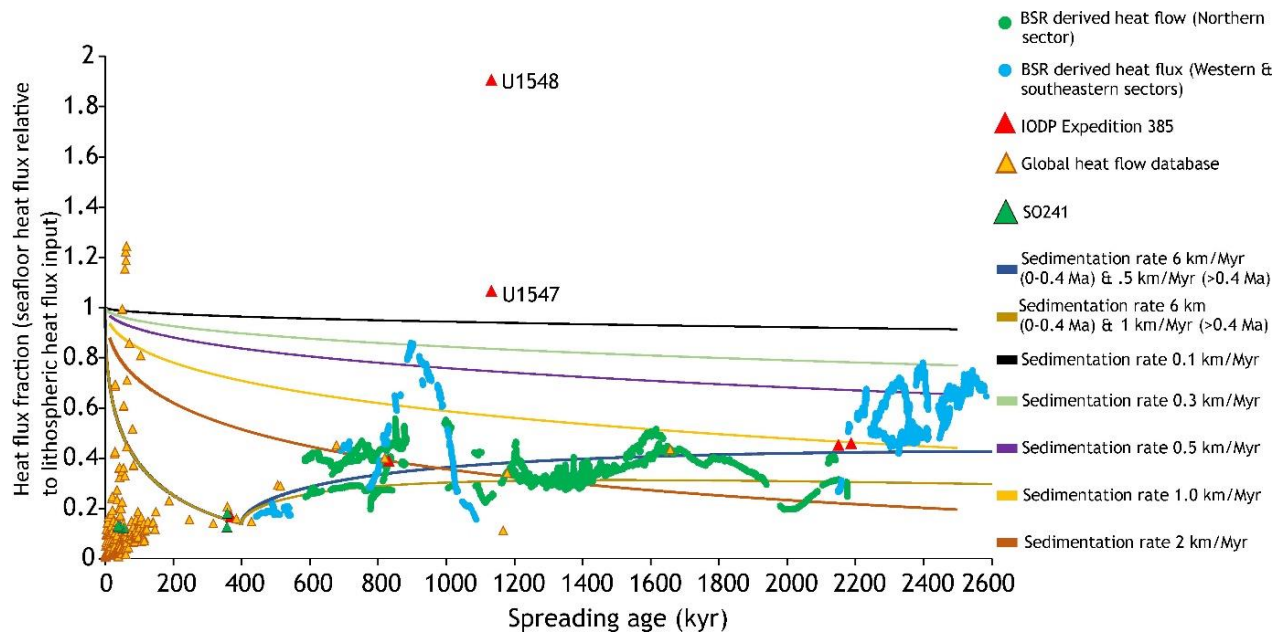
Figure 11. *Seafloor heat flow fraction versus spreading age shows heat flow suppression caused by sedimentation in the northwestern off-axis of the Guaymas Basin. The data points are the compilation of measured heat flow values from the global heat flow database, SO241 heat flow survey, IODP Expedition 385, and BSR derived heat flow values. Solid lines are modeled reference curves depicting heat flow suppression caused by sedimentation. Spreading age is obtained by dividing the distance from the centre of the axial trough by the half-spreading rate.*

Rapid deposition of thick colder sediments can cause a pronounced surface heat flow reduction. In the axial trough, the sediment accumulation rate is extremely high, 3–5 km/Myr (Calvert, 1966; Fisher and Becker, 1991). Using the 1-D heat transfer modeling code SlugSed (Hutnak & Fisher, 2007), we calculate the surface heat flow by considering both constant (3, 2, 1, 0.5, 0.3, 0.1 km/Myr) and time-varying sedimentation rates (6 km/Myr over a younger crust that is <400 kyr old and 0.5–1 km/Myr for the older crust). A substantial fraction (45%) of the measured surface heat flow values in the axial trough is <200 mW/m^2 (heat flow fraction <0.2) and is less than the sedimentation-corrected (6 km/Myr) heat flow in the central axial trough (**Figure 11**). The low values indicate efficient advective removal of heat by the vent complexes that are locally exposed or efficient recharge in those areas. In the poorly consolidated porous and low-permeability sediments, sill intrusion can lead to fluidization, remobilization of sediments, and build-up of high fluid pressure that can trigger the formation of the vent complexes. As the crust spreads away, it experiences a lower sedimentation rate off axis (0.5–1.0 km/Myr), and the surface heat flow trend generally follows the modeled sedimentation (0.5–1 km/Myr)-corrected heat flow on the younger oceanic lithosphere (spreading age 0.4–2 Myr). There is strong variability in the heat flow values in the northwestern areas of the basin outside the axial trough (**Figure 11**). It may indicate the advection of warm fluids in some areas of the basin.

The BSR-derived geothermal gradients decrease from the central basin to the Guaymas Transform margin (**Figure 6**). The values suggest a 43% decline closer to the northern margin than the central off-axis. High sedimentation in the northwestern off-axis region adjacent to the Guaymas Transform margin could cause low heat flow. There is evidence of steep scarps and slumping along the Guaymas Transform (Kluesner et al., 2014). The initial half-graben structure of the northwestern basin formed due to both strike-slip and dip-slip movement along the Guaymas Transform Fault (Aragón- Arreola et al., 2005). Sediment accumulation was greatest in the deeper parts of the half-graben that experienced the greatest subsidence, south of the Guaymas Transform. The unit bound by reflector X and the seafloor is thicker in the northern region than the central off-axis area (**Supporting Figure S9**), resulting in the highest reduction of the geothermal gradient. Sedimentation in the off-axis is variable (0.3–1 km/Myr). The increase in sedimentation rate from 0.3 km/Myr to 1 km/Myr can

suppress the heat flow by 30% on the young lithosphere. We explore additional factors explaining the reduction.

The adjacent northern continental block north of the Guaymas Transform margin may act as a heat sink resulting in lateral conductive heat loss from the hot basin. Lawver and Williams (1979) suggested that heat loss is stronger towards the edge of a new oceanic basin adjacent to the continental block during the first 1 Myr. It can account for an additional reduction in heat flow at the periphery compared to the central off-axis region. A similar process was invoked for the observed absence of magmatism on the Vøring Transform Margin off Norway (Berndt et al., 2001). In addition, the transform margin may facilitate seawater recharge through the fault scarps.

The basin interior is affected by a mass transport complex. Below the mass transport complex, the BSR is slightly deeper than the surrounding areas yielding a lower geothermal gradient (**Supporting Figure S5**). The 2 m-thick top drape over the mass transport complex indicates that the emplacement of the mass transport complex is relatively recent. Its emplacement could have locally depressed the geothermal gradient, and the anomaly suggests that the thermal state is not in steady-state yet.

5.3. Effects of fluid advection on heat-flow, and BSR depth

There is evidence of repeated past hydrothermal venting through the fluid pipes in the southeastern and central regions. We schematically illustrate it in **Figure 12**. It is due to multiple phases of magmatic intrusions, such as Phase-I (~160–200 kyr), Phase-II (~70–100 kyr), and Phase-III (~6–25 kyr). Numerous vent complexes on the seafloor in the central region (within 35 km from the northern axial trough) are likely due to more recent intrusions (Phase-III).

In the northern BSR region, we find short-wavelength thermal anomalies revealed by the undulating and shoaling BSR (**Figures 13a and 13b**). Modeling shows that the wavy pattern is not due to topographic effects (**Figures 13c and 13d**). The low geothermal gradients could be due to recharge or high sedimentation that suppresses the heat flow. The shoaling of the BSR is likely due to fluid upwelling that brings heat closer to the surface, perturbing the BGHS. We find evidence of seismic chimneys that terminate at the buried hydrothermal vent complexes (**Figure 13a**). We infer the vertical fluid flow velocity required to shoal the BGHS by adopting the analytical solution of the 1-D steady-state coupled conduction-advection equation for heat transport (Bredehoeft and Papadopulos, 1965). For this, we assume the average thermal diffusivity and conductivity are 0.5×10^{-6} m^{2}s^{-1} and 1 W/mK, respectively. The thermal conductivity of deeper sediments is slightly greater than that of shallow sediments (0.73 W/mK). At Site U1545 (IODP Expedition 385) thermal conductivity gradually increases with depth (0.73 W/mK at 20 mbsf to 0.9 W/mK at 400 mbsf) (Teske et al., 2021d). To determine the upward fluid flow rate, we assume a steady-state background geothermal gradient of 225° C/km based on the depth of the BSR away from the anomalous hot spots and measured geothermal gradient from the IODP Expedition 385 (Teske et al., 2021d).
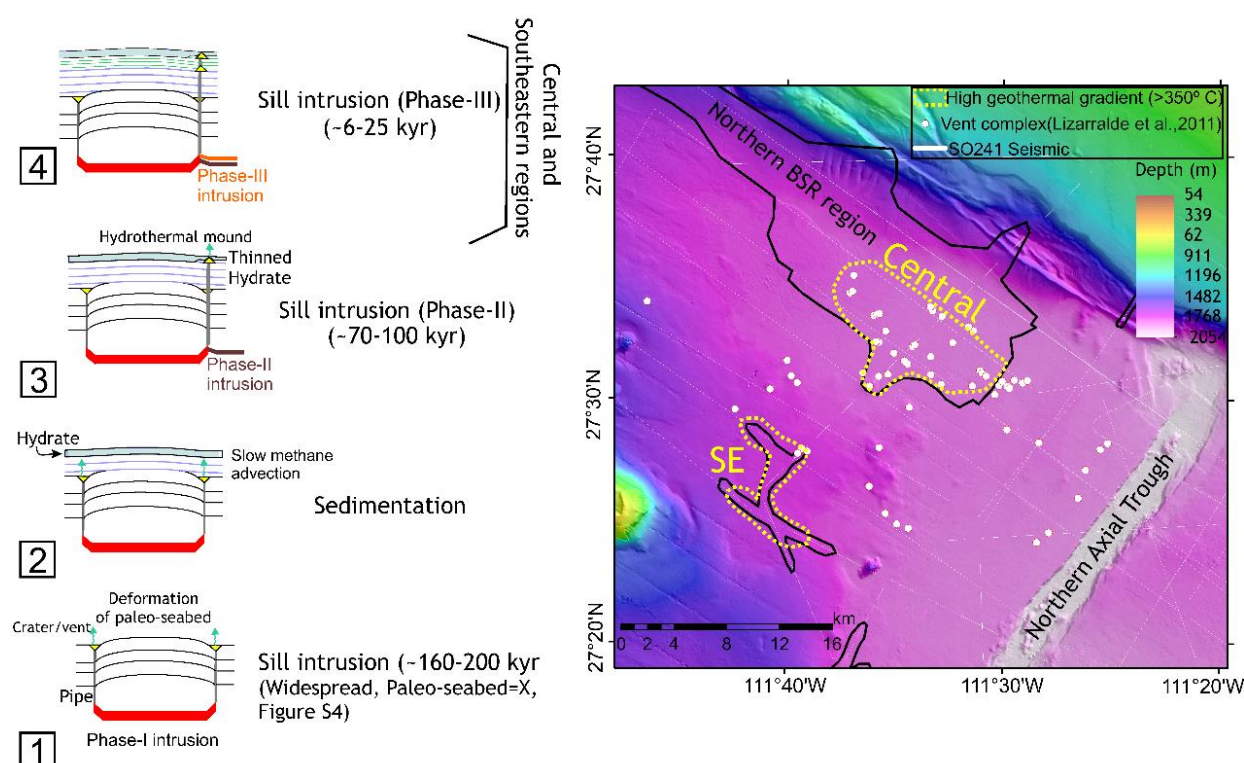
Figure 12. *Multiphase magmatic intrusions in the Guaymas Basin. (**Left**) Schematic illustration summarizing the magmatic and hydrothermal events in the northwestern off-axis. (1) Widespread sill intrusions (Phase-I) caused deformation of the paleo-seafloor (X, Figure S4) and hydrothermal venting (~200–160 kyr). (2) A period of probable off-axis magmatic quiescence during which the vent complexes were buried and hydrate formed. (3) Phase-II magmatic episode and hydrothermal venting took place around 70–100 kyr. The hydrate layer locally thinned due to heating caused by sill intrusion. (4) Phase-III intrusions and hydrothermal venting took place around 6–25 kyr. Numerous vents on the present-day seafloor are clustered in the central region (Lizarralde et al., 2011). The regions with high BSR-derived geothermal gradient (>350° C, Figures 8a and 8b) are marked by yellow polygon and overlap with the locations of seafloor vent complexes (Lizarralde et al., 2011). (**Right**) Basemap showing the areas with high geothermal gradients (>350° C, Figures 8a and 8b) in the central and southeastern (SE) regions.*
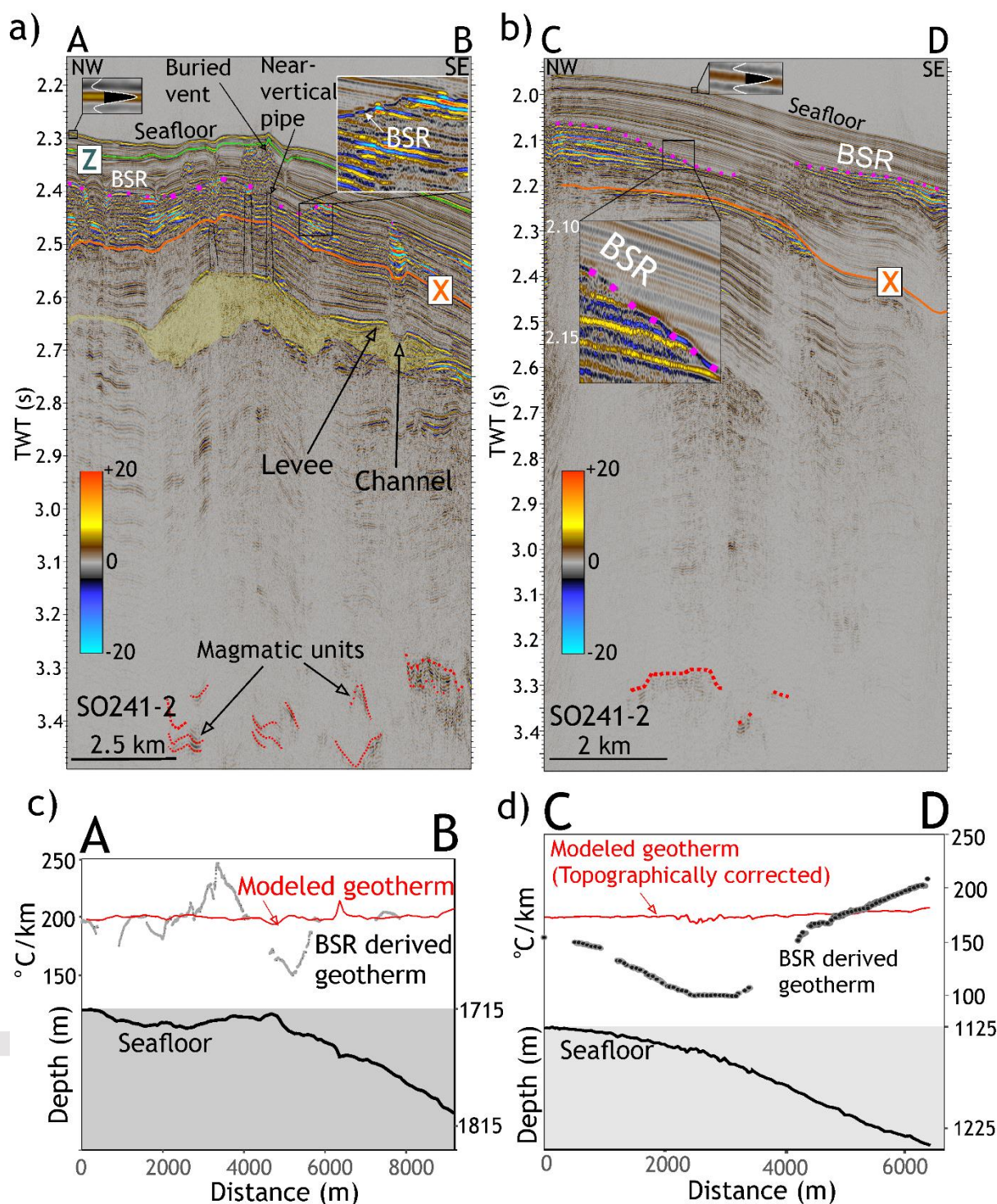
Figure 13. *The BSR in the northern region shows wavy patterns. (a) The seismic line shows shoaling of the BSR, vent complex, buried channel system, and deeper magmatic units (3.3–3.4 s, TWT). A few near-vertical seismic chimneys are present below the buried vent complex. (b) An undulating BSR in seismic line SO241-2. (c) The BSR derived geothermal gradient along the seismic profile is shown in Figure 13a. Modeled geothermal gradients are calculated using a 3-D FEA method. The undulation in BSR derived geothermal gradient is not due to topographic effects. (d) BSR derived geothermal gradient and the modeled geothermal gradient considering the topographic effects along the seismic line CD (Figure 13b). The variation in BSR derived geothermal gradient is not due to the topographic effects. There could be local variations in sedimentation or advection of warm fluid and cold-water recharge that caused the undulation. Seismic line locations are shown in Figure 1.*

Using the seismic data, we constrain the vertical advective flow path length. From the height of the seismic chimney below the vent complex, we assume that the flow path length is 115 m below the convex upward BSR (**Figure 13a**). We find that a fluid upwelling rate of 12 m/kyr is required to shoal the BSR to a depth of 60 mbsf (**Figures S10 and 13a**). As a maximum estimate, we consider a flow path length of 900 m, assuming that fluids can originate from the deeper magmatic units (**Figure 13a**). In that case, the upward fluid upwelling rate is 8 m/kyr. These results are similar to the methane advection rate (<1 cm/yr) reported at the extinct hydrothermal conduits in the northern area (Geilert et al., 2018). The upwelling rates indicate slow advection in the northern regions of the basin. The estimate of fluid upwelling rate is not corrected for sedimentation. Sedimentation can reduce the efficiency of advective heat extraction. The areas where high advective heat transfer counteracts the heat suppression effect of rapid sedimentation appear as hot spots (**Figure 5**).

The southeastern BSR region shows considerable variation in geothermal gradient (74–650° C/km, **Figures 5 and 8b**). There is a convex upward BSR, and the geothermal gradient shows a substantial lateral variation, for example, a change of 500° C/km over 5 km (**Figure 14**). In our view, this pattern can only be explained by heat transfer caused by upwelling fluids and faster advection than at the northern site.

Wang et al. (2009) found low shear wave velocities at 40–90 km below the seafloor in the northwestern areas of the Guaymas Basin. The low-velocity anomalies likely represent centres of buoyancy-driven mantle upwelling caused by the reduced density of the upper mantle from where melt has been extracted. Alternatively, the off-axis low seismic velocity anomalies can also be interpreted as areas of enhanced melt concentration without off-axis upwelling. Mantle upwelling and melting primarily occur at the rift centre, and melt extraction is more efficient in the axial trough than off-axis. The South Guaymas fracture zone (Figure 1, Batiza, 1978) may facilitate melt migration from the spreading centre to off-axis.
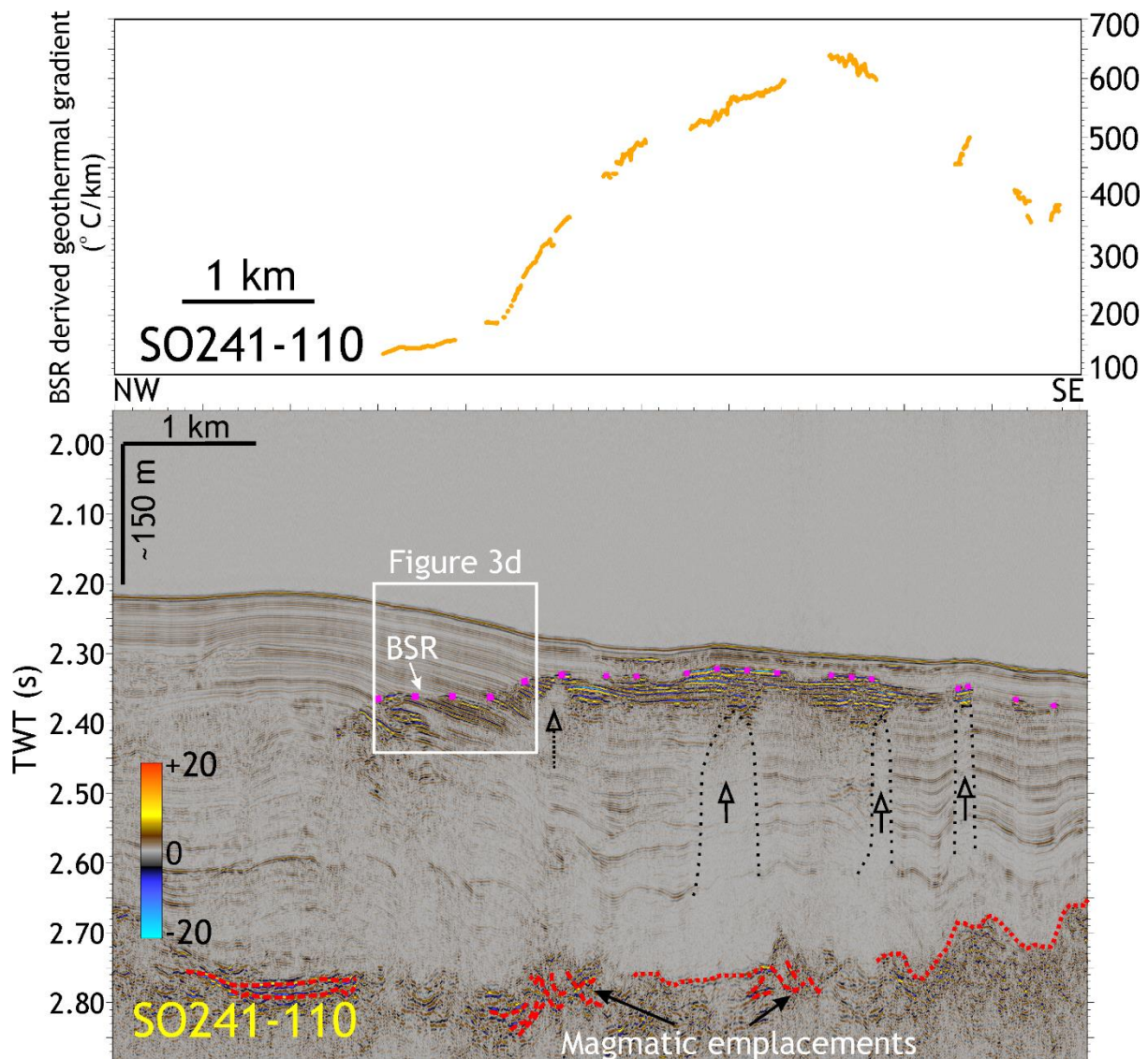
Figure 14. *Seismic line showing a convex upward BSR and considerable lateral variation in geothermal gradient. (**Top**) The convex upward geothermal gradient indicates the role of fluid advection. (**Bottom**) The seismic line shows the magmatic emplacements at 2.65–2.85 s TWT. Several near-vertical zones of amplitude fading (vertical arrows) are inferred as fluid flow conduits that facilitate vertical fluid migration. The shoaling of the BSR could be due to high advective fluxes. The location of the seismic line is shown in Figure 1.*

5.4. Climate Effects

The release of carbon from sedimentary basins by hydrothermal processes is relevant for climate change since the methane can be rapidly injected into the hydrosphere and the atmosphere. Widespread magmatic intrusion and hydrothermal circulation up to approximately 50 km from the spreading centre facilitated carbon release. Higher rates of fluid upwelling during the initial stage of the life cycle of a hydrothermal system can counteract the heat flow suppression effect of sedimentation and result in thermal hot spots on the surface. However, sedimentation effects start to dominate as the advective heat extraction process slows down during the waning stage of hydrothermal activity. Hydrate could form during episodes of magmatic inactivity. Thermal perturbation caused by magmatic intrusions and early-stage hydrothermal activity can thin the earlier formed hydrate layer. Away from the spreading centre, methane is presently stored in gas hydrates that prevent the methane from escaping into the ocean. The fact that upwelling of warm fluids significantly changes the sub-bottom depth of hydrate stability suggests that magmatic intrusions can

release carbon by not only contact metamorphism (Svensen et al., 2004) but they can also lead to hydrate dissociation. It should be considered in mass balance calculations when calculating the volumes of past carbon release during global warming events linked with break-up volcanism (Archer and Buffet, 2005; Dickens, 2011).

6. Conclusions

The surface heat flow as a function of age provides important constraints on the thermal evolution of lithospheric plates (McKenzie, 1967; Turcotte & Oxburgh, 1967). Until now, the understanding of the thermal state of the northwestern Guaymas Basin off-axis region was limited due to few heat flow measurements. Seismic evidence, in the form of a negative polarity BSR, indicates gas hydrate occurrence over larger areas of the basin, such as the northern region located immediately south of the Guaymas Transform and the southeastern and western areas adjacent to the Tortuga Island. Assuming steady-state methane hydrate stability, the BSR-derived geothermal gradient reveals high variability, ranging from 98° to 645° C/km.

Cooling effects due to rapid sedimentation can strongly influence the heat flow in a young oceanic basin near a continent. Heat flow suppression by 20–60% can be caused by very high sedimentation in the axial trough (2–6 km/Myr). Farther away from the axial trough, the plate experiences lower sedimentation rates (0.3–1 km/Myr). Overall, the heat flow values are less than the conductive lithospheric heat flow predictions. The areas adjacent to the Guaymas Transform margin are relatively colder than the central region due to its proximity to the continental block that acts as a heat sink and high sedimentation caused by slumping at the Guaymas Transform. Moreover, there may be possible recharge through the fault scarps. The recent deposition of mass transport complex in the basin's interior has depressed the geothermal gradient.

The BSR-derived geothermal gradient increases with decreasing depth of the magmatic units that are shallower than ~700 mbsf. The correlation is negligible in the northern area, where the magmatic units are much deeper (>700 mbsf). The lack of correlation between the geothermal gradient and the depth of the magmatic units indicates that the magmatic intrusions are likely to have cooled down to a large extent. Near some buried vent complexes in the northern area, the BSR shows a gentle shoaling caused by slow fluid upwelling.

The southeastern region shows much higher geothermal gradients than elsewhere in the off-axis areas of the Guaymas Basin. The hot spots characterized by the steep lateral gradient are near the west-northwest trending Tortuga Volcanic Ridge . The presence of deeper magmatic units and near-vertical seismic chimneys indicate the role of magmatic intrusions that trigger the advection of hot fluids. More recent magmatic emplacement can substantially heat the sediments and explain the very high thermal anomaly in the southeastern region.

Open Research

References

Aarnes, I., Svensen, H., Connolly, J. A. D., & Podladchikov, Y. Y. (2010). How contact metamorphism can trigger global climate changes: Modeling gas generation around igneous sills in sedimentary basins. Geochimica et Cosmochimica Acta, 74, 7179–7195. https://doi.org/10.1016/j.gca.2010.09.011.

Aragón-Arreola, M., Morandi, M., Martín-Barajas, A., Delgado-Argote, L., & González-Fernández, A. (2005). Structure of the rift basins in the central Gulf of California: Kinematic implications for oblique rifting. *Tectonophysics*, 409, 19–38. https://doi.org/10.1016/j.tecto.2005.08.002.

Archer, D., and Buffett, B. (2005), Time-dependent response of the global ocean clathrate reservoir to climatic and anthropogenic forcing, Geochem. Geophys. Geosyst., 6, Q03002, doi:10.1029/2004GC000854.

Batiza, R. (1978). Geology, petrology, and geochemistry of Isla Tortuga, a recently formed tholeiitic island in the Gulf of California. *Bulletin of the Geological Society of America*, 89(9), 1309–1324. https://doi.org/10.1130/0016-7606(1978)89<1309:GPAGOI>2.0.CO;2.

Berndt, C., Hensen, C., Mortera-Gutierrez, C., Sarkar, S., Geilert, S., Schmidt, M., et al. (2016). Rifting under steam-How rift magmatism triggers methane venting from sedimentary basins. *Geology*, 44(9), 767–770. https://doi.org/10.1130/G38049.1.

Berndt, C., Mjelde, R., Planke, S. et al. (2001). Controls on the tectono-magmatic evolution of a volcanic transform margin: the Vøring Transform Margin, NE Atlantic. *Marine Geophysical Researches,* 22, 133–152. https://doi.org/10.1023/A:1012089532282.

Bray, N. A. (1988). Thermohaline circulation in the Gulf of California. *Journal of Geophysical Research,* 93(C5), 4993–5020. https://doi.org/10.1029/JC093iC05p04993.

Bredehoeft, J. D., & Papaopulos, I. S. (1965). Rates of vertical groundwater movement estimated from the Earth's thermal profile. *Water Resources Research,* 1(2), 325–328. https://doi.org/10.1029/WR001i002p00325.

Calvert, S. E. (1966). Origin of Diatom-Rich, Varved Sediments from the Gulf of California. *The Journal of Geology*, 74, 546–565. https://doi.org/10.1086/627188.

Chi, W.-C., Reed, D. L. (2008). Evolution of shallow, crustal thermal structure from subduction to collision: An example from Taiwan. *GSA Bulletin*, 120 (5-6), 679–690. https://doi.org/10.1130/B26210.1

Claypool G. E., Kaplan I. R. (1974). The Origin and Distribution of Methane in Marine Sediments. In: Kaplan I.R. (eds) Natural Gases in Marine Sediments. Marine Science, 3. Springer, Boston, MA. https://doi.org/10.1007/978-1-4684-2757-8_8.

Curray, J. R., Moore, D. G., Kelts, K., & Einsele, G. (1982). Tectonics and geological history of the passive continental margin at the tip of Baja California (DSDP, Leg 64). *Initial reports DSDP. Leg 64, Mazatlan to Long Beach, 1978-79,* 1089–1116.

Davis, E. E., Chapman, D. S., Wang, K., Villinger, H., Fisher, A. T., Robinson, S. W., et al. (1999). Regional heat flow variations across the sedimented Juan de Fuca Ridge eastern flank: Constraints on lithospheric cooling and lateral hydrothermal heat transport. *Journal of Geophysical Research: Solid Earth,* 104(B8), 17675–17688.

https://doi.org/10.1029/1999JB900124.

De La Lanza-Espino, G., & Soto, L. A. (1999). Sedimentary geochemistry of hydrothermal vents in Guaymas Basin, Gulf of California, Mexico. *Applied Geochemistry,* 14, 499–510. https://doi.org/10.1016/S0883-2927(98)00064-X.

Dickens, G. R. (2011), Down the rabbit hole: Toward appropriate discussion of methane release from gas hydrate systems during the Paleocene–Eocene thermal maximum and other past hyperthermal events, Clim. Past, 7, 831–846, doi:10.5194/cp-7-831-2011.

Didyk, B. M., & Simoneit, B. R. T. (1989). Hydrothermal oil of Guaymas Basin and implications for petroleum formation mechanisms. *Nature*, 342, 65–69. https://doi.org/10.1038/342065a0.

Einsele, G. (1985). Basaltic sill-sediment complexes in young spreading centers: Genesis and significance. *Geology* 13(4), 249–252. https://doi.org/10.1130/0091-7613(1985)13<249:BSCIYS>2.0.CO;2.

Einsele, G., Gieskes, J. M., Curray, J., Moore, D. M., Aguayo, E., Aubry, M. P., et al. (1980). Intrusion of basaltic sills into highly porous sediments, and resulting hydrothermal activity. *Nature,* 283, 441–445. https://doi.org/10.1038/283441a0.

Einsele, G., & Kelts, K. (1982). Pliocene and Quaternary mud turbidites in the Gulf of California: sedimentology, mass physical properties and significance. *Initial reports DSDP, Leg 64, Mazatlan to Long Beach, 1978–79.* 511–528.

Elder, J.W. (1965). Physical Processes in Geothermal Areas. In Terrestrial Heat Flow, W.H.K. Lee (Ed.). https://doi.org/10.1029/GM008p0211.

Fabriol, H., Delgado-Argote, L. A., Dañobeitia, J. J., Córdoba, D., González, A., García-Abdeslem, J., et al. (1999). Backscattering and geophysical features of volcanic ridges offshore Santa Rosalia, Baja California Sur, Gulf of California, Mexico. *Journal of Volcanology and Geothermal Research,* 93, 75–92. https://doi.org/10.1016/S0377-0273(99)00084-0.

Fisher, A. T., & Becker, K. (1991). Heat flow, hydrothermal circulation and basalt intrusions in the Guaymas Basin, Gulf of California. *Earth and Planetary Science Letters,* 103, 84–99. https://doi.org/10.1016/0012-821X(91)90152-8.

Fisher, A. T., & Narasimhan, T. N. (1991). Numerical simulations of hydrothermal circulation resulting from basalt intrusions in a buried spreading center. *Earth and Planetary Science Letters,* 103, 100–115. https://doi.org/10.1016/0012-821X(91)90153-9.

Galerne, C.Y., and Hasenclever, J. (2019). Distinct Degassing Pulses During Magma Invasion in the Stratified Karoo Basin – New Insights From Hydrothermal Fluid Flow Modeling. Geochemistry, Geophysics, Geosystems, 20. https://doi.org/10.1029/2018GC008120.

Ganguly, N., Spence, G. D., Chapman, N. R, & Hyndman, R. D. (2000). Heat flow variations from bottom simulating reflectors on the Cascadia margin. *Marine Geology*, Volume 164, Issues 1–2, Pages 53–68. https://doi.org/10.1016/S0025-3227(99)00126-7.

Geilert, S., Hensen, C., Schmidt, M., Liebetrau, V., Scholz, F., Doll, M., et al. (2018). Transition from hydrothermal vents to cold seeps records timing of carbon release in the Guaymas Basin, Gulf of California. *Biogeosciences,* 15, 5715–5731.

Grove, C., (2013). Submarine hydrothermal vent complexes in the Paleocene of the Faroe-Shetland Basin: Insights from three-dimensional seismic and petrographical data. *Geology,* 41(1), 71–74. https://doi.org/10.1130/G33559.1.

Haacke, R. R., Hyndman, R. D., Park, K-P., Yoo, D-G., Stoian, I., & Schmidt, U. (2009). Migration and venting of deep gases into the ocean through hydrate-choked chimneys offshore Korea. *Geology,* 37(6), 531–534. doi: https://doi.org/10.1130/G25681A.1.

Hamilton, R.V. and Minshell, B.J., (2019). Hydrothermal vents and seismic anomalies: implications for the petroleum system NE of Shetland. *Petroleum Geoscience,* 25(1), 90–101. https://doi.org/10.1144/petgeo2017-072.

Hartmann, A., & Villinger, H. (2002). Inversion of marine heat flow measurements by expansion of the temperature decay function. *Geophysical Journal International*, 148, 628–636. https://doi.org/10.1046/j.1365-246X.2002.01600.x.

Hayba, D. O., and Ingebritsen, S. E. (1997). Multiphase groundwater flow near cooling plutons, J. Geophys. Res., 102(B6), 12235–12252. https://doi.org/10.1029/97JB00552.

He, T., Spence, G. D., Riedel, M., Hyndman, R. D., & Chapman, N. R. (2007). Fluid flow and origin of a carbonate mound offshore Vancouver Island: Seismic and heat flow constraints. *Marine*

Geology, 239, 83–98. https://doi.org/10.1016/j.margeo.2007.01.002.

Hornbach, M. J., Ruppel, C., Saffer, D. M., Van Dover, C. L., & Holbrook, W. S. (2005). Coupled geophysical constraints on heat flow and fluid flux at a salt diapir, *Geophys. Res. Lett.*, 32, L24617. doi:10.1029/2005GL024862.

Hutnak, M., & Fisher, A. T. (2007). Influence of sedimentation, local and regional hydrothermal circulation, and thermal rebound on measurements of seafloor heat flux. *Journal of Geophysical Research: Solid Earth,* 112, B12101. https://doi.org/10.1029/2007JB005022.

Hyndman, R. D., Davis, E. E., & Wright, J. A. (1979). The measurement of marine geothermal heat flow by a multipenetration probe with digital acoustic telemetry and insitu thermal conductivity. *Marine Geophysical Researches,* 4, 181–205.

Iyer, K., Rüpke, L., and Galerne, C. Y. (2013), Modeling fluid flow in sedimentary basins with sill intrusions: Implications for hydrothermal venting and climate change, Geochem. Geophys. Geosyst., 14, 5244– 5262, doi:10.1002/2013GC005012.

Jamtveit, B., Svensen, H., Podladchikov, Y. Y., & Planke, S. (2004). Hydrothermal vent complexes associated with sill intrusions in sedimentary basins. Geological Society Special Publication, 234, 233–241. https://doi.org/10.1144/GSL.SP.2004.234.01.15.

Kipp, K. L., Hsieh, P. A. and Charlton, S. R. (2008) Guide to the Revised Ground-Water Flow and Heat Transport Simulator : HYDROTHERM—Version 3, U.S. Geological Survey, (Techniques and Methods 6-A25), p. 160.

Kjoberg, S., Schmiedel, T., Planke, S., Svensen, H.H., Millett, J.M., Jerram, D.A., Galland, O., Lecomte, I., Schofield, N., Haug, Ø.T. and Helsem, A., (2017). 3D structure and formation of hydrothermal vent complexes at the Paleocene-Eocene transition, the Møre Basin, mid-Norwegian margin. *Interpretation,* 5(3), SK65-SK81. https://doi.org/10.1190/INT-2016-0159.1.

Kluesner, J., Lonsdale, P., & González-Fernández, A. (2014). Late Pleistocene cyclicity of sedimentation and spreading-center structure in the Central Gulf of California. *Marine Geology*, 347, 58–68. https://doi.org/10.1016/j.margeo.2013.11.001.

Kolandaivelu, K. P., Harris, R. N., Lowell, R. P., Robinson, A. H., Wilson, D. J., & Hobbs, R. W. (2020). Evolution of heat flow, hydrothermal circulation and permeability on the young southern flank of the Costa Rica Rift. *Geophysical Journal International*, 220, 278–295, https://doi.org/10.1093/gji/ggz278.

Kvenvolden, K. A. (1993). Gas hydrates—geological perspective and global change, Rev. Geophys., 31(2), 173–187, https://doi.org/10.1029/93RG00268.

Langseth, M. G., & Von Herzen, R. P. (1970). Heatflow through the floor of the world oceans. In: The Sea, vol. 4, part 1. (A. E. Maxwell, Ed.) Wiley-Interscience, NY, pp. 299–352.

Larson, R. L., Menard, H. W., & Smith, S. M. (1968). Gulf of California: A result of ocean-floor spreading and transform faulting. *Science,* 161, 781–784. https://doi.org/10.1126/science.161.3843.781.

Lawver, L. A., Sclater, J. G., Henyey, T. L., & Rogers, J. (1973). Heat flow measurements in the southern portion of the Gulf of California. *Earth and Planetary Science Letters,* 19, 198–208, https://doi.org/10.1016/0012-821X(73)90115-5.

Lawver, L. A., & Williams, D. L. (1979). Heat flow in the Central Gulf of California. *Journal of Geophysical Research*, 84(B7), 3465– 3478. https://doi.org/10.1029/JB084iB07p03465.

Lin, Y. S., Koch, B. P., Feseker, T., Ziervogel, K., Goldhammer, T., Schmidt, F., et al. (2017). Near-surface heating of young rift sediment causes mass production and discharge of reactive dissolved organic matter. *Scientific Reports*, 7, 44864. https://doi.org/10.1038/srep44864.

Lizarralde, D., Axen, G. J., Brown, H. E., Fletcher, J. M., González-Fernández, A., Harding, A. J., et al. (2007). Variation in styles of rifting in the Gulf of California. *Nature*, 448, 466–469. https://doi.org/10.1038/nature06035.

Lizarralde, D., Soule, S. A., Seewald, J. S., & Proskurowski, G. (2011). Carbon release by off-axis magmatism in a young sedimented spreading centre. *Nature Geoscience,* 4, 50–54. https://doi.org/10.1038/ngeo1006.

Lonsdale, P. (1985). A Transform Continental Margin Rich in Hydrocarbons, Gulf of California. *American Association of Petroleum Geologists Bulletin*, 69 (7), 1160–1180. https://doi.org/10.1306/AD462BA0-16F7-11D7-8645000102C1865D.

Lonsdale, P., & Becker, K. (1985). Hydrothermal plumes, hot springs, and conductive heat flow in the Southern Trough of Guaymas Basin. *Earth and Planetary Science Letters*, 73, 211–225, https://doi.org/10.1016/0012-821X(85)90070-6.

Magee, C., Jackson, C.L. and Schofield, N. (2014). Diachronous sub- volcanic intrusion along deep-water margins: Insights from the Irish Rockall Basin. *Basin Research,* 26(1), 85–105. https://doi.org/10.1111/bre.12044.

McKenzie, D. P. (1967). Some remarks on heat flow and gravity anomalies. *Journal of Geophysical Research*, 72(24), 6261–6273. https://doi.org/10.1029/JZ072i024p06261.

Omosanya, K.O., Eruteya, O.E., Siregar, E.S., Zieba, K.J., Johansen, S.E., Alves, T.M. and Waldmann, N.D. (2018). Three-dimensional (3-D) seismic imaging of conduits and radial faults associated with hydrothermal vent complexes (Vøring Basin, Offshore Norway). *Marine Geology,* 399, 115–134. https://doi.org/10.1016/j.margeo.2018.02.007.

Padilla y Sánchez, R.J., Domínguez Trejo, I., López Azcárraga, A. G., Mota Nieto, J., Fuentes Menes, A. O., Rosique Naranjo, F., Germán Castelán, E. A., Campos Arriola, S. E. (2013). National Autonomous University of Mexico Tectonic Map of Mexico GIS Project, American Association of Petroleum Geologists GIS Open Files series.

Paull, C. K., Caress, D. W., Thomas, H., Lundsten, E., Anderson, K., Gwiazda, R., et al. (2015). Seafloor geomorphic manifestations of gas venting and shallow subbottom gas hydrate occurrences. *Geosphere*, 11(2), 491–513. https://doi.org/10.1130/GES01012.1.

Planke, S., Rasmussen, T., Rey, S. S., & Myklebust, R. (2005). Seismic characteristics and distribution of volcanic intrusions and hydrothermal vent complexes in the Vøring and Møre basins. Geological Society Special Publication, Petroleum Geology Conference series, 6, 833–844. https://doi.org/10.1144/0060833.

Portnov, A., Cook, A. E., & Vadakkepuliyambatta, S. (2021). Diverse gas composition controls the Moby-Dick gas hydrate system in the Gulf of Mexico. *Geology*, 49(12), 1446–1451. doi: https://doi.org/10.1130/G49310.1.

Ratcliffe, E. H. (1960). The thermal conductivities of ocean sediments. *Journal of Geophysical Research,* 65, 1535–1541.

Reynolds, P., Planke, S., Millett, J.M., Jerram, D.A., Trulsvik, M., Schofield, N. and Myklebust, R. (2017). Hydrothermal vent complexes offshore Northeast Greenland: A potential role in driving the PETM. *Earth and Planetary Science Letters,* 467, 72–78. https://doi.org/10.1016/j.epsl.2017.03.031.

Robles, J. M., & Marinone, S. G. (1987). Seasonal and interannual thermohaline variability in the Guaymas Basin of the Gulf of California. *Continental Shelf Research*, 7, 715–733. https://doi.org/10.1016/0278-4343(87)90013-6.

Roelofse, C, Alves, TM, Omosanya, K.O. (2021). Reutilisation of hydrothermal vent complexes for focused fluid flow on continental margins (Modgunn Arch, Norwegian Sea). *Basin Res.*, 33, 1111–1134. https://doi.org/10.1111/bre.12507.

Roussel, E. G., Bonavita, M. A. C., Querellou, J., Cragg, B. A., Webster, G., Prieur, D., & Parkes, R. J. (2008). Extending the sub-sea-floor biosphere. *Science*, 320, 1046, https://doi.org/10.1126/science.1154545.

Schmiedel, T., Kjoberg, S., Planke, S., Magee, C., Galland, O., Schofield, N., Jackson, C.A.L. and Jerram, D.A. (2017). Mechanisms of overburden deformation associated with the emplacement of the Tulipan sill, mid-Norwegian margin. *Interpretation*, 5(3), SK23-SK38. https://doi.org/10.1190/INT-2016-0155.1.

Schofield, N., Holford, S., Millett, J., Brown, D., Jolley, D., Passey, S.R., Muirhead, D., Grove, C., Magee, C., Murray, J. and Hole, M. (2017). Regional magma plumbing and emplacement mechanisms of the Faroe- Shetland Sill Complex: implications for magma transport and petroleum systems within sedimentary basins. *Basin Research,* 29(1), 41-63. https://doi.org/10.1111/bre.12164.

Shipboard Scientific Party DSDP 64 (1982). Curray, J. R., Moore, D. G., et al., Init. Repts. DSDP, 64, 211–415, Washington (U.S. Govt. Printing Office), doi: 10.2973/dsdp.proc.64.1982.

Shipley, T. H., M. H. Houston, R. T. Buffler, F. J. Shaub, K. J. McMillen, J. W. Ladd, and J. L. Worzel (1979), Seismic evidence for widespread possible gas hydrate horizons on continental

slopes and rises, AAPG Bull., 63(12), 2204–2213. https://doi.org/10.1306/2F91890A-16CE-11D7-8645000102C1865D.

Simoneit, B. R. T., & Lonsdale, P. F. (1982). Hydrothermal petroleum in mineralized mounds at the seabed of Guaymas Basin. *Nature*, 295, 198–202. https://doi.org/10.1038/295198a0.

Skogseid, J., Pedersen, T., Eldholm, O., & Larsen, B. T. (1992). Tectonism and magmatism during NE Atlantic continental break-up: The Vøring Margin. *Geological Society Special Publication*, 68, 305–320. https://doi.org/10.1144/GSL.SP.1992.068.01.19.

Sloan, E. D., (1998). Clathrate Hydrates of Natural Gases, *Second Edition*. Marcel Dekker, NY.

Sloan, E. D., and Koh, C. A. (2008). Clathrate Hydrates of Natural Gases, *3rd Edn.* New York, NY: CRC Press.

Strasser, M., Moore, G. F., Kimura, G., Kitamura, Y., Kopf, A. J., Lallemant, S., et al. (2009). Origin and evolution of a splay fault in the Nankai accretionary wedge. *Nature Geoscience,* 2, 648–652. https://doi.org/10.1038/ngeo609.

Svensen, H., Jamtveit, B., Planke, S., & Chevallier, L. (2006). Structure and evolution of hydrothermal vent complexes in the Karoo Basin, South Africa. Journal of the Geological Society, 163, 671–682. https://doi.org/10.1144/1144-764905-037.

Svenson, H., Planke, S., Maithe-Sørensen, A., Jamtveit, B., Myklebust, R., Eidem, T. R., & Rey, S. S. (2004). Release of methane from a volcanic basin as a mechanism for initial Eocene global warming. *Nature,* 429, 542–545. https://doi.org/10.1038/nature02566.

Taner, M. T., Schuelke, J. S., O'Doherty, R., & Baysal, E. (1994). Seismic attributed revisited. *SEG Technical Program Expanded Abstracts 1994*, SL2.5, 1104–1106. https://doi.org/10.1190/1.1822709.

Teske, A., Callaghan, A. V., & LaRowe, D. E. (2014). Biosphere frontiers of subsurface life in the sedimented hydrothermal system of Guaymas Basin. *Frontiers in Microbiology,* 5. https://doi.org/10.3389/fmicb.2014.00362.

Teske, A., De Beer, D., McKay, L. J., Tivey, M. K., Biddle, J. F., Hoer, D., et al. (2016). The Guaymas Basin hiking guide to hydrothermal mounds, chimneys, and microbial mats: Complex seafloor expressions of subsurface hydrothermal circulation. *Frontiers in Microbiology,* 7. https://doi.org/10.3389/fmicb.2016.00075.

Teske, A., McKay, L. J., Ravelo, A. C., Aiello, I., Mortera, C., Núñez-Useche, F., et al. (2019). Characteristics and Evolution of sill-driven off-axis hydrothermalism in Guaymas Basin – the Ringvent site. In *Scientific Reports,* 9, 13847. https://doi.org/10.1038/s41598-019-50200-5.

Teske, A., Lizarralde, D., Höfig, T.W., Aiello, I.W., Ash, J.L., Bojanova, D.P., Buatier, M.D., Edgcomb, V.P., Galerne, C.Y., Gontharet, S., Heuer, V.B., Jiang, S., Kars, M.A.C., Khogenkumar Singh, S., Kim, J.-H., Koornneef, L.M.T., Marsaglia, K.M., Meyer, N.R., Morono, Y., Negrete-Aranda, R., Neumann, F., Pastor, L.C., Peña-Salinas, M.E., Pérez Cruz, L.L., Ran, L., Riboulleau, A., Sarao, J.A., Schubert, F., Stock, J.M., Toffin, L.M.A.A., Xie, W., Yamanaka, T., and Zhuang, G. (2021a). Expedition 385 Summary. Proceedings of the International Ocean Discovery Program Volume 385. Publications.iodp.org. https://doi.org/10.14379/iodp.proc.385.101.2021.

Teske, A., Lizarralde, D., Höfig, T.W., Aiello, I.W., Ash, J.L., Bojanova, D.P., Buatier, M.D., Edgcomb, V.P., Galerne, C.Y., Gontharet, S., Heuer, V.B., Jiang, S., Kars, M.A.C., Khogenkumar Singh, S., Kim, J.-H., Koornneef, L.M.T., Marsaglia, K.M., Meyer, N.R., Morono, Y., Negrete-Aranda, R., Neumann, F., Pastor, L.C., Peña-Salinas, M.E., Pérez Cruz, L.L., Ran, L., Riboulleau, A., Sarao, J.A., Schubert, F., Stock, J.M., Toffin, L.M.A.A., Xie, W., Yamanaka, T., and Zhuang, G. (2021b). Expedition 385 methods. Proceedings of the International Ocean Discovery Program Volume 385. Publications.iodp.org. https://doi.org/10.14379/iodp.proc.385.102.2021.

Teske, A., Lizarralde, D., Höfig, T.W., Aiello, I.W., Ash, J.L., Bojanova, D.P., Buatier, M.D., Edgcomb, V.P., Galerne, C.Y., Gontharet, S., Heuer, V.B., Jiang, S., Kars, M.A.C., Khogenkumar Singh, S., Kim, J.-H., Koornneef, L.M.T., Marsaglia, K.M., Meyer, N.R., Morono, Y., Negrete-Aranda, R., Neumann, F., Pastor, L.C., Peña-Salinas, M.E., Pérez Cruz, L.L., Ran, L., Riboulleau, A., Sarao, J.A., Schubert, F., Stock, J.M., Toffin, L.M.A.A., Xie, W., Yamanaka, T., and Zhuang, G. (2021c). Sites U1547 and U1548. In Teske, A.,

Lizarralde, D., Höfig, T.W., and the Expedition 385 Scientists, Guaymas Basin Tectonics and Biosphere. Proceedings of the International Ocean Discovery Program, 385: College Station, TX (International Ocean Discovery Program). https://doi.org/10.14379/iodp.proc.385.105.2021.

Teske, A., Lizarralde, D., Höfig, T.W., Aiello, I.W., Ash, J.L., Bojanova, D.P., Buatier, M.D., Edgcomb, V.P., Galerne, C.Y., Gontharet, S., Heuer, V.B., Jiang, S., Kars, M.A.C., Khogenkumar Singh, S., Kim, J.-H., Koornneef, L.M.T., Marsaglia, K.M., Meyer, N.R., Morono, Y., Negrete-Aranda, R., Neumann, F., Pastor, L.C., Peña-Salinas, M.E., Pérez Cruz, L.L., Ran, L., Riboulleau, A., Sarao, J.A., Schubert, F., Stock, J.M., Toffin, L.M.A.A., Xie, W., Yamanaka, T., and Zhuang, G. (2021d). Sites U1545. Proceedings of the International Ocean Discovery Program Volume 385. Publications.iodp.org. https://doi.org/10.14379/iodp.proc.385.103.2021.

Turcotte, D. L., & Oxburgh, E. R. (1967). Finite amplitude convective cells and continental drift. *Journal of Fluid Mechanics*, 28, 29–42, https://doi.org/10.1017/S0022112067001880.

Von Herzen, R., & Maxwell, A. E. (1959). The measurement of thermal conductivity of deep-sea sediments by a needle-probe method. *Journal of Geophysical Research*, 64, 1557–1563.

Wang, Y., Forsyth, D. W., & Savage, B. (2009). Convective upwelling in the mantle beneath the Gulf of California. *Nature*, 462, 499–501. https://doi.org/10.1038/nature08552.

White, R. S. (1979). Gas hydrate layers trapping free gas in the Gulf of Oman. *Earth and Planetary Science Letters*, 42, 114–120. https://doi.org/10.1016/0012-821X(79)90196-1.

Williams, D. L., Becker, K., Lawver, L. A., & Von Herzen, R. P. (1979). Heat flow at the spreading centers of the Guaymas Basin, Gulf of California. *Journal of Geophysical Research*, 84(B12), 6757– 6769. https://doi.org/10.1029/JB084iB12p06757.

Yamano, M., Uyeda, S., Aoki, Y., & Shipley, T. H. (1982). Estimates of heat flow derived from gas hydrates. *Geology,* 10(7), 339–343. https://doi.org/10.1130/0091-7613(1982)10<339:EOHFDF>2.0.CO;2.

Zander, T., Haeckel, M., Berndt, C., Chi, W.-C., Klaucke, I., Bialas, J., Klaeschen, D., Koch, S., & Atgin, O. (2017). On the origin of multiple BSRs in the Danube deep-sea fan, Black Sea. *Earth and Planetary Science Letters*, Volume 462, 15–25. https://doi.org/10.1016/j.epsl.2017.01.006.